Solar wind - magnetosphere coupling during radial IMF conditions: simultaneous multi-point observations

Sergio Toledo-Redondo[1], Kyoung-Joo Hwang[2], Christopher Philippe Escoubet[3], Benoit Lavraud[4], Jesús Fornieles[5], Nicolas Aunai[6], Robert C Fear[7], Jérémy Dargent[8], Huishan Fu[9], Stephen A. Fuselier[2], Kevin J Genestreti[2], Yuri V. Khotyaintsev[10], Wenya Li[11], Cecilia Norgren[12], and Tai-Duc Phan[13]

[1]Department of Electromagnetism and Electronics, University of Murcia
[2]Southwest Research Institute
[3]ESA / ESTEC
[4]Institut de Recherche en Astrophysique et Planetologie - CNRS
[5]University of Granada
[6]IRAP, Toulouse, France
[7]University of Southampton
[8]Università di Pisa
[9]Beihang University
[10]Swedish Institute of Space Physics
[11]National Space Science Center, Chinese Academy of Sciences
[12]Department of Physics and Technology, University of Bergen
[13]UC Berkeley

November 21, 2022

Abstract

In situ spacecraft missions are powerful assets to study processes that occur in space plasmas. One of their main limitations, however, is extrapolating such local measurements to the global scales of the system. To overcome this problem at least partially, multi-point measurements can be used. There are several multi-spacecraft missions currently operating in the Earth's magnetosphere, and the simultaneous use of the data collected by them provides new insights into the large-scale properties and evolution of magnetospheric plasma processes. In this work, we focus on studying the Earth's magnetopause using a conjunction between the MMS and Cluster fleets, when both missions skimmed the magnetopause for several hours at distant locations during radial IMF conditions. The observed magnetopause positions as a function of the evolving solar wind conditions and compared to model predictions of the magnetopause. We observe an inflation of the magnetosphere (0.7 R_E), consistent with magnetosheath pressure decrease during radial IMF conditions, which is less pronounced on the flank ($<$ 0.2 R_E). There is observational evidence of magnetic reconnection in the subsolar region for the whole encounter, and in the dusk flank for the last portion of the encounter, suggesting that reconnection was extending more than 15 R_E. However, reconnection jets were not always observed, suggesting that reconnection was patchy, intermittent or both. Shear flows reduce the reconnection rate up to 30% in the dusk flank according to predictions, and the plasma ß enhancement in the magnetosheath during radial IMF favors reconnection suppression by the diamagnetic drift.

Solar wind - magnetosphere coupling during radial IMF conditions: simultaneous multi-point observations

S. Toledo-Redondo[1,2], K.-J. Hwang[3], C. P. Escoubet[4], B. Lavraud[5,2], J. Fornieles[6], N. Aunai[7], R. C. Fear[8], J. Dargent[9], H. Fu[10], S. A. Fuselier[3,11], K. J. Genestreti[12], Yu. V. Khotyaintsev[13], Wy. Li[14], C. Norgren[15], and T. D. Phan[16]

[1]Department of Electromagnetism and Electronics, University of Murcia, Murcia, Spain.
[2]Institut de Recherche en Astrophysique et Planétologie, Université de Toulouse, CNRS, UPS, CNES, Toulouse, France.
[3]Southwest Research Institute, San Antonio, Texas, USA.
[4]ESA, European Space Research and Technology Centre, Noordwijk, Netherlands.
[5]Laboratoire d'Astrophysique de Bordeaux, Univ. Bordeaux, CNRS, B18N, allée Geoffroy Saint-Hilaire, 33615 Pessac, France
[6]Department of Electromagnetism and Matter Physics, University of Granada, Granada, Spain.
[7]UMR7648 Laboratoire de physique des plasmas (LPP), Palaiseau, France.
[8]School of Physics and Astronomy, University of Southampton, Southampton, United Kingdom.
[9]Institut für Theoretische Physik, Ruhr-Universität Bochum, Bochum, Germany.
[10]School of Space and Environment, Beihang University, Beijing, China.
[11]Department of Physics and Astronomy, University of Texas at San Antonio, San Antonio, TX, USA.
[12]Southwest Research Institute, Durham, NH, USA.
[13]Swedish institute of Space Physics, Uppsala, Sweden.
[14]State Key Laboratory of Space Weather, National Space Science Center, Chinese Academy of Sciences, Beijing, 100190, China.
[15]University of Bergen, Bergen, Norway.
[16]SSL, University of California, Berkeley, CA 94720, USA.

Key Points:

- Simultaneous observations of the equatorial magnetopause in the subsolar region and dusk flank during time-extended radial IMF
- The magnetopause position is shifted ∼0.7 R_E in the subsolar region and <0.2 R_E in the flank compared to models
- Simultaneous reconnection evidence suggests extended reconnection along more than 15 R_E during part of the encounter

Corresponding author: S. Toledo-Redondo, `sergio.toledo@um.es`

Abstract

In situ spacecraft missions are powerful assets to study processes that occur in space plasmas. One of their main limitations, however, is extrapolating such local measurements to the global scales of the system. To overcome this problem at least partially, multi-point measurements can be used. There are several multi-spacecraft missions currently operating in the Earth's magnetosphere, and the simultaneous use of the data collected by them provides new insights into the large-scale properties and evolution of magnetospheric plasma processes. In this work, we focus on studying the Earth's magnetopause using a conjunction between the MMS and Cluster fleets, when both missions skimmed the magnetopause for several hours at distant locations during radial IMF conditions. The observed magnetopause positions as a function of the evolving solar wind conditions and compared to model predictions of the magnetopause. We observe an inflation of the magnetosphere ($\sim$0.7 R_E), consistent with magnetosheath pressure decrease during radial IMF conditions, which is less pronounced on the flank (< 0.2 R_E). There is observational evidence of magnetic reconnection in the subsolar region for the whole encounter, and in the dusk flank for the last portion of the encounter, suggesting that reconnection was extending more than 15 R_E. However, reconnection jets were not always observed, suggesting that reconnection was patchy, intermittent or both. Shear flows reduce the reconnection rate up to $\sim$30 % in the dusk flank according to predictions, and the plasma β enhancement in the magnetosheath during radial IMF favors reconnection suppression by the diamagnetic drift.

1 Introduction

The Earth's magnetopause (MP) is the boundary between the Earth's magnetosphere, dominated by the Earth's intrinsic magnetic field, and the shocked solar wind, i.e. the magnetosheath, dominated by the Sun's intrinsic magnetic field. Its location and shape depends mainly on upstream solar wind conditions, and the magnetopause has been subject of study during the last decades, both using numerical simulations (e.g., Palmroth et al., 2001; Wiltberger et al., 2003; Lu et al., 2011, 2013) and empirical models built from in-situ spacecraft observations (e.g., D. H. Fairfield, 1971; Sibeck et al., 1991; Boardsen et al., 2000; Safrankova et al., 2002; Petrinec & Russell, 1996; Shue et al., 1998; Lin et al., 2010; Dusik et al., 2010; Wang et al., 2013).

The model reported by Shue et al. (1998) (S98) is a widely used magnetopause model, based on 553 magnetopause crossings. It uses a simple analytical form and assumes a symmetric magnetopause around the GSE X axis. It depends on two parameters: the solar wind dynamic pressure (P_d) and the magnitude of the Z component of the Interplanetary Magnetic Field (IMF) (B_z). Its functional form is

$$r = r_0 \left(\frac{2}{1 + cos\theta} \right)^{\alpha} \tag{1}$$

where r is the radial distance to the Earth's center, and θ is the solar zenith angle. α and r_0 are found empirically as a function of IMF B_z and solar wind dynamic pressure. The predictions of this model are similar to the predictions by Petrinec and Russell (1996) (PR96), another widely used axisymmetric model. Case and Wild (2013) estimated, using more than 2700 crossings of the Cluster spacecraft (polar orbit), spanning more than 8 years, that on average these two models tend to overestimate the radial distance between the magnetopause and the Earth center by $\sim$1 R$_E$ (9%).

Since the S98 and PR96 models are axisymmetric, they cannot account for cusp indentations, and are expected to produce deviations at high latitudes. The model reported by Lin et al. (2010) (L2010) is another empirical model, where the asymmetry of the MP and the effect of the dipole tilt are considered. As additional inputs, it uses the IMF magnetic pressure (P_m) and the dipole tilt (Φ). They employed 2708 magnetopause crossings from multiple spacecraft to build their model, which uses 21 free parameters. Case and Wild (2013) estimated, using the same database mentioned above, that the radial magnetopause distance was underestimated, on average, by $\sim$0.25 R$_E$ (2.3%). Other non-axisymmetric models present in the literature are for instance Boardsen et al. (2000); Wang et al. (2013).

Samsonov et al. (2016) performed an exhaustive model comparison, including 8 empirical models and 7 MHD models. They concluded that empirical models yield differences in radial distance of the order of 1 R$_E$ between themselves. Depending on the solar wind upstream conditions, different models may provide better predictions than others, whose accuracy also depends on the magnetopause latitude. For instance, the L10 model provides the best predictions for the case $B_z = 0$, and these predictions are very close to MHD models. They also noted that none of the models is designed to account for radial IMF conditions, when the magnetopause location drifts towards the Sun (D. Fairfield et al., 1990; Merka et al., 2003).

Radial IMF conditions (IMF cone angles <25° or >155°), represent $\sim$15% of observations at 1 AU (Suvorova et al., 2010; Pi et al., 2014), although they have received much less attention than northward and southward IMF conditions. For radial IMF, a quasi-parallel bow shock in the subsolar region is formed, resulting in lower magnetic pressure exerted on the magnetosphere. In addition, the dynamic pressure of the solar wind is usually small for radial IMF ($P_d < 1.5$ nPa) (e.g., Park et al., 2016), plus the magnetosheath dynamic pressure becomes even smaller than in the solar wind, partly due the increase of reflected ions in the quasi-parallel bow shock. Therefore, the total pressure that the magnetosphere experiences is much smaller than for IMF cone angles close to 90°, and as a result the magnetopause expands towards the Sun. Merka et al. (2003), based on a two-point magnetopause observation event, proposed a bullet-shaped expansion of the magnetosphere for radial IMF, featuring an expansion towards the Sun in the subsolar region and thinning in the flanks. By contrast, Dusik et al. (2010) proposed a global expansion of the magnetosphere during radial IMF, featuring an inflation both in the subsolar region and in the flanks, based on statistical observations ($\sim$6,500 MP crossings from THEMIS) during radial IMF.

Dusik et al. (2010) also reported that the PR96 empirical model tends to underestimate the radial position of the magnetopause, in particular when the IMF has a large radial component, from $\sim$0.3 R$_E$ for cone angle of 90° to $\sim$1.7 R$_E$ for cone angle close to 0° or 180°. They attributed it to a decrease in the effective dynamic pressure exerted at the boundary. Samsonov et al. (2012) studied the effective total pressure reduction over the magnetopause using MHD simulations and THEMIS observations. They concluded that the total pressure is reduced by $\sim$24% when the IMF cone angle is close to 0° or 180°. Suvorova and Dmitriev (2015) compared various magnetopause models and concluded that for low solar wind dynamic pressure conditions ($P_d < 0.3$ nPa), typical of radial IMF conditions, L2010 model performed better than S98 and PR96 models, although none of these models could account for the magnetosheath P_d reduction with respect to P_d in the solar wind for radial IMF.

The coupling between the Earth's magnetosphere and the solar wind is largely controlled by magnetic reconnection, which is most efficient during southward IMF conditions, i.e., the magnetic flux density reconnected per unit time maximizes. The amount of energy transferred to the Earth's magnetosphere system depends on the efficiency of this coupling, which is governed by both the reconnection rate and the extent of the X line. Cassak and Shay (2007) found scaling relations of the reconnection rate for asymmetric reconnection, which have been tested both using numerical simulations and statistical observations. The denser magnetosheath dominates the hybrid Alfvén velocity and controls, to a large extent, the reconnection rate (e.g., Borovsky, 2008; Lavraud & Borovsky, 2008; Borovsky et al., 2013; S. A. Fuselier et al., 2017). In the presence of cold ions of ionospheric origin, the outer dayside magnetosphere sometimes can have densities similar to magnetosheath densities, which also impact the reconnection rate (Borovsky & Denton, 2006; Walsh et al., 2013; S. A. Fuselier, Mukherjee, et al., 2019; S. A. Fuselier, Trattner, et al., 2019; S. A. Fuselier et al., 2021; Dargent et al., 2020).

The extent of the X line at the magnetopause has been constrained using spacecraft conjunctions by a number of studies, most of them during southward IMF conditions. There have been various studies that made use of simultaneous multi-point observations during southward IMF, and have reported extended X line lengths at the magnetopause, with measured minimum lengths ranging from 2 to 9 Earth radii (R_E), and potentially extending longer distances (Phan et al., 2000; Marchaudon et al., 2005; Berchem et al., 2008; Fear et al., 2009; Dunlop et al., 2011; Kitamura et al., 2016). Similarly, Phan et al. (2006) reported an X line extending at least 8 R_E during B_y IMF. On the other hand, Walsh et al. (2017) used simultaneous (less than 1 minute) observations of the magnetopause on two THEMIS spacecraft separated by 3.9 Earth radii in the Y$_{GSM}$ direction. They found signatures of reconnection (jets) only in one of the spacecraft, challenging the model of an extended X line as predicted by MHD global simulations. The situation they found is consistent with either spatially patchy reconnection or a spatially limited X line. Reconnection switching on and off in time is not consistent with their observations owing to the simultaneity of the measurements. The IMF was southward but the cone angle for this event was $\sim 50°$.

Although what controls the extent of the X line at the magnetopause is not fully understood, there are two mechanisms that are expected to suppress magnetic reconnection locally: shear flows and diamagnetic drifts along the reconnection jet direction. Cowley and Owen (1989) indicated that magnetic reconnection should be suppressed if the flow shear velocity parallel to the jet direction exceeds twice the Alfvén speed of the magnetosheath. La Belle-Hamer et al. (1995) suggested that twice the largest Alfvén speed (magnetosphere or magnetosheath) would be the critical speed for determining reconnecting suppression by shear flows. For symmetric reconnection, Cassak and Otto (2011) found that if the shear flow exceeds the Alfvén speed, reconnection is suppressed. Their simulations provided a scaling law for the reconnection rate

$$E \sim E_0 \left(1 - \frac{v_s^2}{v_A^2}\right), \tag{2}$$

where E and E_0 correspond to the reconnecting electric field with and without correction for the shear flow reduction, v_s is the shear flow speed in the outflow direction, and v_A is the Alfvén speed.

More recently, C. E. Doss et al. (2015) extended the formulation in Equation 2 to the case of asymmetric magnetic reconnection. They showed, using two-fluid simulations, that asymmetric reconnection may be more difficult to suppress by shear flows when the asymmetry is large, as it is the case at the magnetopause:

$$E_{asym} \sim E_{0,asym} \left(1 - \frac{v_s^2}{v_{A,asym}^2} \frac{4\rho_1 B_2 \rho_2 B_1}{(\rho_1 B_2 + \rho_2 B_1)^2}\right), \tag{3}$$

where E_{asym} and $E_{0,asym}$ correspond to the resulting reconnecting electric field with and without correction for the shear flow in asymmetric reconnection, $v_{A,asym}$ is the hybrid Alfvén speed (Cassak & Shay, 2007), ρ is the mass density, B is the magnetic field strength, and subscripts 1 and 2 stand for each region adjacent to the reconnecting current sheet. This prediction has been shown to hold in Particle-In-Cell simulations (C. Doss et al., 2016). Equation 3 may have implications for our current understanding on how planetary magnetospheres interact with the solar wind. For instance in Saturn, shear flow suppression has been considered a major suppression mechanism by e.g., Desroche et al. (2013). However, Sawyer et al. (2019) did not find evidence of reconnection suppression by shear flows at Saturn.

Another mechanism that is known to be able to suppress magnetic reconnection is the diamagnetic drift of the reconnection X line (along the outflow direction) dure to pressure gradients across the current sheet. The condition for reconnection suppression is that the diamagnetic drift speed exceeds the Alfvén velocity (Swisdak et al., 2003, 2010). This suppression condition is often expressed as

$$\Delta\beta > 2(L/d_i)\tan(\theta/2), \quad (4)$$

where $\Delta\beta$ is the change in plasma β across the current sheet, L is the current sheet width, d_i is the ion skin depth and θ is the magnetic field shear angle across the current sheet at the reconnection site. Vernisse et al. (2020) noted that, strictly speaking, $\Delta\beta$ should be calculated using only the normal to the current sheet component of the pressure tensor (P_{nn} in LMN coordinates) and the guide field component of the magnetic field (B_M in LMN coordinates), although typically the total plasma β is considered. Tests of reconnection suppression by the diamagnetic drift at the magnetopause of Earth (Phan et al., 2013) and Saturn (S. Fuselier et al., 2020) have been largely successful. Equation 4 indicates that this suppression mechanism is at work mainly for large guide field configurations or large asymmetries in the plasma inflow.

This manuscript is organized as follows. In section 2, we describe the MMS and Cluster orbits during the magnetopause conjunction, its configuration and the main plasma properties during the event. In section 3, we compare our observations to two model predictions of the magnetopause location simultaneously in the flank and the subsolar region. In section 4, we assess the occurrence of magnetic reconnection based on observations and compare it to the predictions of the reconnection suppression mechanisms. Finally, in section 5, we discuss and summarize the main findings of this study.

2 Description of the MMS - Cluster magnetopause conjunctions on 28-11-2016

The Cluster mission (Escoubet et al., 2001) was launched in 2001 into an elliptical polar orbit with the aim of surveying multiple magnetospheric regions. It is composed of four identical spacecraft that have been flying in multiple configurations, e.g., tetrahedron or string of pearls, at different length-scales, from few km (electron scale) to several thousand km (MHD scale). In this work, we use measurements from FGM (Balogh et al., 1997), and CIS-CODIF (Reme et al., 2001).

The MMS mission (Burch et al., 2015) was launched in 2015 with the aim of studying magnetic reconnection at the Earth's magnetopause and magnetotail, with a focus on the associated kinetic-scale processes. It is a suite of four identical spacecraft flying in tetrahedron formation, to distinguish time from spatial variations. Each spacecraft has several instruments to measure plasma parameters. In this work, we use the flux gate magnetometers (Russell et al., 2014) and FPI (Fast Plasma Instrument) to measure electrons and ions (Pollock et al., 2016).

On 28th November 2016, both the Cluster and MMS fleets were skimming the magnetopause simultaneously for several hours. Cluster was in the dusk flank near the terminator and MMS was near the subsolar region, at roughly (0, 15, 0) and (8, 5, 1) Earth radii (R_E) in GSE coordinates, respectively. The Cluster and MMS position in the interval 09:00 - 18:00 UT is shown in Figures 1a, 1b and 1c, in the GSE XZ, XY, and YZ planes, respectively. C1 and C2 were at 0.5 R_E of separation and C3 and C4 at 0.4 R_E of separation, and the distance between the two groups was of $\sim$1.1 R_E. On the other hand, all four MMS spacecraft were in close ($\sim$10 km) tetrahedron formation. For the rest of this work, all MMS measurements are taken from MMS1 and are representative of the other MMS spacecraft observations. During the MMS - Cluster conjunction studied here, the solar wind speed was roughly 400 km/s (not shown), and the Interplanetary magnetic field (IMF) was dominated by GSE X component ($\mathbf{B}_{IMF} \simeq B_x$, Figures

1d and 1e). The solar wind conditions remained roughly stable between 09:00 - 14:00 UT. After that time, there is a **B** field rotation in Y and the dynamic pressure started increasing, from ∼1.5 nPa at 14:00 UT to more than 3 nPa at 18:00UT (Figure 1f), and the IMF cone angle (θ_{CA}) started fluctuating. The next two panels show an overview of the observations made by MMS. Figure 1g shows MMS measured magnetic field in GSE coordinates. When MMS is in the magnetosphere, near the subsolar region, **B** is dominated by $B_z \simeq 40$ nT. Figure 1h shows the FPI ion omnidirectional spectrogram observed by MMS. The magnetosphere regions show high-energy ions at several keV, corresponding to the dayside plasma sheet population. A cold ion component of ionospheric origin is also detected by FPI most of the time in the magnetosphere, at few tens of eV (visible between 14:00 - 14:30 UT in Figure 1h). In the magnetosheath, the ion energies are of the order of several hundred eV to few keV. Figure 1i shows **B** field measurements in the dusk flank from C4 during the same time interval. B_z is positive at times when Cluster is in the magnetosphere, and $B_m \simeq 30$ nT, where subscript m stands for magnetosphere. Figure 1j shows the CODIF H^+ omnidirectional spectrogram measured by C4. It corresponds to the unique ion measurement available on the cluster fleet during the conjunction. The magnetospheric plasma sheet ion population, with energies avove 10 keV, shows similar density and temperature in the flank (Cluster) and in the subsolar region (MMS). The magnetosheath ion population, on the other hand, shows lower density in the flank (not shown). Vertical black lines correspond to the times when a conjunction between any of the Cluster and MMS spacecraft was identified. We define the conjunctions when both the MMS fleet and at least one of the Cluster spacecraft cross the magnetopause current sheet within an interval of less than 5 minutes. Using this criterion, we identify 15 conjunctions that are summarized in Table 1, corresponding to red numbers and vertical black lines in Figure 1e. Some of the conjunctions correspond to full crossings and some to partial crossings. Some of them are clean, single crossings, but others may correspond to multiple crossings within a short (less than 5 min) time interval.

3 Location and shape of the magnetopause

The observations of the magnetopause reported in Table 1 allow us to test current models of the magnetopause simultaneously at distant locations. We focus on two empirical models: S98 (Shue et al., 1998) and L10 (Lin et al., 2010). These models do not depend on IMF cone angle, and to account for the effect of the extended radial IMF observed during the conjunction, we use the effective magnetosheath pressure reduction reported by Samsonov et al. (2012), scaled linearly as a function of the IMF cone angle (θ_{CA}):

$$P_{d,sheath} = (0.76 + 0.121\theta_{CA})P_{d,SW}, \tag{5}$$

where θ_{CA} varies between 0 - $\pi/2$. In the following, we compare the two magnetopause models with and without applying this correction (subscript c and no subscript, respectively), to test these results simultaneously both in the subsolar region and in the flank.

Table 2 shows the upstream solar wind conditions from the OMNI database, i.e., propagated to the bow shock (P_d, P_m, B_z, B_x/B) and the value of the dipole tilt (Φ) for the 15 crossings reported in Table 1. Using these input values, we computed the MP location for S98 and L10 models, with and without the correction for the dynamic pressure (subscript c for corrected pressure) suggested by Samsonov et al. (2012). Table 2 also shows the distance of MMS constellation and C4 to the MP models. A negative sign corresponds to $r_{model} < r_{sc}$. The distance between the observed location of the MP and the location predicted by each model are summarized in Figure 2. The mean distance over the 15 simultaneous crossings is plotted using circles, and the error bars correspond to one standard deviation. At the flank magnetopause, both S98 and L10 underestimate the measured MP position by less than 0.2 R_E. The corrected models for radial IMF overestimate the measured flank MP position by ∼0.4 R_E. On the other hand, in the subsolar region the models S98 and L10 underestimate the MP position by $\sim$0.8 R_E and $\sim$0.6 R_E respectively, while the corrected models S98$_c$ and L10$_c$ lead to underestimates of $\sim$0.4 R_E and $\sim$0.2 R_E, respectively. The corrections for radial IMF yield better results in the subsolar region, with the model L10$_c$ as the most accurate one.

Figure 3a shows the MMS (red) and C4 (blue) orbits during the 9-hour interval. Red and blue dots correspond to each of the 15 MP crossings of Tables 1 and 2 for MMS and C4, respectively. The black and green curves correspond to the S98 and L10 MP models corresponding to the solar wind conditions at the beginning of the time interval in Figure 1. The Figures 3b-g show details of crossings 2, 13 and 15 and the MP models for the solar wind conditions at the time of each event, for MMS (red) and C4 (blue).

4 Magnetic reconnection at the subsolar and dusk flank magnetopause

Next, we take the events of Table 1 that have full MP crossings for both MMS and C4 (i.e., events 3, 5, 6, 8, 9, 10, 11 and 15) and apply Minimum Variance Analysis (MVA) to the magnetic field. The N direction obtained in the subsolar region and in the flank is roughly consistent with the MP model predictions, except for event 9, which is discarded. For each of these events, we search for observational evidence of ongoing reconnection based on two criteria: presence of reconnection jets in the L direction and the existence of electron only Low Latitude Boundary layer (eLLBL) earthward of the magnetopause (Gosling et al., 1990). We also estimate and compare the conditions on both sides of the magnetopause (magnetosphere, *sp*, and magnetosheath, *sh*) simultaneously in the subsolar region (MMS) and at the dusk flank (C4), which allow us to test the theoretical conditions for reconnection suppression discussed in the introduction (Equations 3 and 4).

Figure 4 shows an example (event 15) on how we proceeded to obtain LMN coordinates, search for reconnection signatures, and obtain the *sp* and *sh* conditions simultaneously in the subsolar region and in the flank. Panels a-e correspond to Cluster (C4) observations, and panels f-j correspond to MMS observations of the same variables, namely magnetic field, ion density, ion velocity, ion spectrogram and electron spectrogram. All vectors are provided in local LMN coordinates, obtained from applying MVA to the **B** field in the yellow-shaded regions, which correspond to the magnetopause crossing. The LMN coordinates are specified in panels a and f, for C4 and MMS, respectively. For both C4 (Figure 4e) and MMS (Figure 4j) we observe magnetosheath electrons earthward of the magnetopause, deeper into the magnetosphere than magnetosheath ions, which suggest that reconnection is ongoing or was ongoing recently. This signature is attributed to a time of flight effect of electrons sitting on an open field line connected to the magnetosheath (Gosling et al., 1990; Vines et al., 2017). We also search for jets in ion velocity (black lines in Figures 4c and 4h) of the order of the Alfvén velocity (listed in Table 3), which would indicate ongoing reconnection. For event 15, the data is not conclusive. Two possible narrow reconnection jets are observed at $\sim$17:48:45UT (Figure 4c, cluster) and $\sim$17:46:36 UT (Figure 4h, MMS), although their peak velocity in the L direction is less than 50% of the predicted Alfvén velocity. The blue-shaded regions correspond to the reference time interval (15 s) for inferring magnetosheath quantities, and the red-shaded regions correspond to the reference time interval (15 s) for inferring magnetospheric quantities. Ion velocities estimated by CIS-CODIF on C4 are not reliable in the magnetosphere due to the low counts, so they have been masked in panel c. We assume that velocity in the flank magnetosphere is negligible compared to flank magnetosheath velocity.

The same analysis explained in Figure 4 for event 15 has been applied to events 3, 5, 6, 8, 10 and 11, and their corresponding Figures are provided in the supplemental material (Figures S1 - S6). The reference magnetosheath and magnetosphere intervals adjacent to the magnetopause crossings allow us to test the theoretical predictions of reconnection suppression by shear flows and the diamagnetic drift. The main parameters (L and N direction, magnetic field and density, hybrid Alfvén velocity, shear flow velocity, $\Delta\beta$ and **B** clock angle) are provided in Table S1 of the supplemental material. Table 3 summarizes the results of the observed reconnection signatures (jets and eLLBL), the expected reduction in reconnection rate due to shear flows, $(E/E_0)_{asym}$, and whether reconnection is expected to be suppressed by the diamagnetic drift of the X line.

4.1 Observational evidence of reconnection

The eLLBL is observed in all MMS crossings, indicating that reconnection in the subsolar region was taking place during the encounter. The eLLBL is also observed by C4 in the flank towards the end of the encounter, for events 11 and 15, and is not observed during events 6 and 8. This suggests that reconnection may be at work locally in the flank only during the late hours of the encounter. Solar wind B_y increases at $\sim$12:50 UT, just before event 10, and the solar wind dynamic pressure also varies, first decreasing (events 10 and 11) and then increasing (event 15), see Figure 1. In addition, events 10 and 11 show southward reconnection jets in the subsolar region (See Figures S5 and S6 of the supplemental material). The direction of the jets is consistent with the expected location of the X line according to the maximum magnetic shear model (Trattner et al., 2007). Overall, the combination of eLLBL and jet identification suggests that reconnection was at work in the subsolar region during the whole encounter, while in the flank reconnection was at work after $\sim$13 UT. No clear jet signatures are identified for all subsolar crossings, but this may be due to various reasons, including intermittent occurrence of reconnection, or the X line being close to the spacecraft position, as for the electron diffusion region event observed by MMS the same day at $\sim$07 UT (Genestreti et al., 2018).

4.2 Suppression of magnetic reconnection by shear flows

In the subsolar region (MMS observations), the L direction corresponds roughly to GSE Z for all the crossings, while the N direction is a combination of GSE X and GSE Y. On the other hand, the L direction is not stable in the dusk flank (C4 observations), with L changing between GSE -X and GSE Z. The N direction in the dusk flank is roughly in GSE Y and GSE X. Table 3 indicates that in the subsolar region, the observed shear flows in the L direction are smaller than the hybrid Alfvén velocity, resulting in negligible (less than 2%) expected reconnection rate reduction, $(E/E_0)_{asym}$, according to Equation 3 (C. E. Doss et al., 2015). On the other hand, the shear flow velocity in the L direction is of the same order or larger than the hybrid Alfvén velocity in the dusk flank for events 5, 6, 8, and 10, resulting in variable expected reconnection reductions, $0.71 < (E/E_0)_{asym} < 0.98$.

4.3 Suppression of magnetic reconnection by diamagnetic drift

We test the Swisdak condition (Equation 4) at each magnetopause crossing from Table 3, and plot the results in Figure 5. The black solid assumes L/d_i=1, and the dashed lines assume $L/d_i = 1/3$ and $L/d_i = 3$. The plasma β in the magnetosheath and magnetosphere correspond to average values of 15 s intervals on each side of the magnetopause current sheet (see Table S1 and Figures S1-6 of the supplemental material). The **B** rotation angle is taken in the plane perpendicular to the magnetopause normal, i. e., the plane that contains L and M directions, computed using MVA on magnetic field data. In contrast with the observational evidence of reconnection described in Section 4.1, we find that reconnection is expected to be suppressed for several of the events, both in the subsolar region and in the dusk flank. We attribute this discrepancy to the fact that the Swisdak test is applied locally, not at the X line location, which is unknown. The plasma β in the subsolar magnetosheath are most of the time well above 1, what would require moderate to large **B** field rotation angles for reconnection to occur, which are not satisfied locally for the events under study. The clock angles and the $\Delta\beta$ are in general smaller in the flank (Cluster observations, blue) than in the subsolar magnetosphere (MMS observations, red), but in both cases they stay in the reconnection suppression region of the plot.

5 Discussion and Conclusion

Park et al. (2016) analyzed 19 years of magnetospheric magnetic field data at geosynchronous orbit and cross-correlated it with magnetic field data of the solar wind at 1 AU. They found that for radial IMF conditions, the magnetospheric magnetic field was systematically smaller than for northward IMF conditions, over all magnetic local times and regardless of season or magnetic latitude. This result is consistent with the model of global expansion of the magnetosphere during radial IMF (Dusik et al., 2010). Our results in Figure 2 are also consistent with this picture, i.e. expansion both at the flanks and the subsolar region, rather than a thinning of the magnetosphere on the flanks. However, the measured expansion is of the order of 0.6 - 0.8 R_E in the subsolar region and <0.2 R_E at the flanks.

The persistent observation of the eLLBL in MMS data indicates that reconnection was at work in the subsolar region. This result is supported by the identification of reconnection jets in events 6, 10 and 11, and possibly in events 5, 8, and 11. By contrast, no jet signatures are present for event 3. The variability of jet observations has two possible explanations: MMS was close to the X line, as for the event reported by Genestreti et al. (2018) few hours before, or reconnection was intermittent in time. Evidence for local reconnection in the dusk flank is also present for events 11 and 15. This is consistent both with an X line extending from the MMS to the C4 location, i.e., more than 15 R_E, or with patchy reconnection involving multiple X lines. On the other hand, reconnection seems not to be at work in the flank magnetopause near the C4 location for events 3, 5, 6, and 8. The solar wind conditions significantly start changing at ∼12:50 UT, between events 9 and 10.

While the L direction in the subsolar region is roughly in the GSE Z direction, in the flank is often oriented in the GSE X direction, i.e, the direction of the magnetosheath flow. We estimate predicted reconnection rate reductions in the flank of 4 - 29% for events 3, 5, 6 and 8, while the rate reduction due to shear flows is negligible in the subsolar region. We note, however, that these calculations consider magnetosphere and magnetosheath references at the spacecraft location, while the conditions at the X line may be different, in particular the L direction.

During radial IMF conditions, the magnetosheath dynamic pressure becomes low, and the magnetic pressure that the magnetosheath exerts on the magnetopause becomes even lower, resulting in an enhanced magnetosheath plasma β (e.g., Le & Russell, 1994; Suvorova et al., 2010; Suvorova & Dmitriev, 2016). The dynamic pressure in the magnetosheath is lower than in the solar wind during radial IMF owing to the quasi-parallel bow shock that is formed in the subsolar region and to the shorter size of the magnetosheath. The resulting magnetosheath β enhancement favors suppression of magnetic reconnection by the diamagnetic drift, as illustrated in Figure 5. However, these results are evaluated at the spacecraft location, not at the X line. In addition, accurate evaluation of Equation 4 requires reliable LMN coordinates. While the L direction determination is robust for our events, the N direction was less robust. The eigenvalue ratio of the intermediate to minimum direction (l_2/l_3) resulting from MVA was small (∼3) for some of the events. The magnetosheath magnetic field orientation and strength is variable during the encounter, as expected behind a quasi-parallel bow shock. Overall, radial IMF conditions may favor time-varying conditions at the magnetopause, which may result in intermittent and spatial and time varying magnetic reconnection. More analysis of radial IMF events is needed to confirm these results.

To summarize, we analyzed an equatorial magnetopause conjunction between MMS (subsolar region) and Cluster (dusk flank) during radial IMF conditions, enabling us to study the meso-scale of the magnetopause using simultaneous in-situ measurements. Our results indicate that the magnetosphere inflates under radial IMF in the subsolar region ($\sim$0.7 R_E) and to a lesser extent in the flank (<0.2 R_E), suggesting a magnetopause deformation in addition to the inflation. Magnetic reconnection was at work in the subsolar region for the whole encounter based on the observed eLLBL, although reconnection jets were not always clearly identified. In the flank, reconnection was at work for the last hours of the encounter, suggesting that the extent of the X line was larger than 15 R_E. However, the magnetosheath **B** is variable during radial IMF, and this may lead to patchy and non-steady magnetic reconnection at the magnetopause.

Acknowledgments

STR and JF acknowledge support of the Ministry of Economy and Competitiveness (MINECO) of Spain (grant FIS2017-90102-R). Research at IRAP was supported by CNRS, CNES and the University of Toulouse. We acknowledge support of the ISSI teams *MMS and Cluster observations of magnetic reconnection* and *Cold plasma of ionospheric in the Earth's magnetosphere*, and of the ESAC Science faculty. The omni database is publicly available at https://omniweb.gsfc.nasa.gov/. The MMS database is publicly available at https://lasp.colorado.edu/mm
The Cluster database is publicly available at https://csa.esac.esa.int/.

References

Balogh, A., Dunlop, M., Cowley, S., Southwood, D., Thomlinson, J., Glassmeier, K., ... Acuna, M. (1997). The cluster magnetic field investigation. *Space Science Reviews*, *79*(1), 65-91.

Berchem, J., Marchaudon, A., Dunlop, M., Escoubet, C., Bosqued, J., Reme, H., ... Carr, C. (2008). Reconnection at the dayside magnetopause: Comparisons of global mhd simulation results with cluster and double star observations. *Journal of Geophysical Research: Space Physics*, *113*(A7).

Boardsen, S., Eastman, T., Sotirelis, T., & Green, J. (2000). An empirical model of the high-latitude magnetopause. *Journal of Geophysical Research: Space Physics*, *105*(A10), 23193-23219.

Borovsky, J. E. (2008). The rudiments of a theory of solar wind/magnetosphere coupling derived from first principles. *Journal of Geophysical Research: Space Physics*, *113*(A8), n/a-n/a.

Borovsky, J. E., & Denton, M. H. (2006). Effect of plasmaspheric drainage plumes on solar-wind/magnetosphere coupling. *Geophysical Research Letters*, *33*(20).

Borovsky, J. E., Denton, M. H., Denton, R. E., Jordanova, V. K., & Krall, J. (2013). Estimating the effects of ionospheric plasma on solar wind/magnetosphere coupling via mass loading of dayside reconnection: Ion-plasma-sheet oxygen, plasmaspheric drainage plumes, and the plasma cloak. *Journal of Geophysical Research: Space Physics*, *118*(9), 5695-5719.

Burch, J. L., Moore, T. E., Torbert, R. B., & Giles, B. L. (2015). Magnetospheric multiscale overview and science objectives. *Space Science Reviews*, *199*(1-4), 5-21.

Case, N., & Wild, J. (2013). The location of the earth's magnetopause: A comparison of modeled position and in situ cluster data. *Journal of Geophysical Research: Space Physics*, *118*(10), 6127-6135.

Cassak, P. A., & Otto, A. (2011). Scaling of the magnetic reconnection rate with symmetric shear flow. *Physics of Plasmas*, *18*(7).

Cassak, P. A., & Shay, M. A. (2007). Scaling of asymmetric magnetic reconnection: General theory and collisional simulations. *Physics of Plasmas*, *14*(10).

Cowley, S., & Owen, C. (1989). A simple illustrative model of open flux tube motion over the dayside magnetopause. *Planetary and space science*, *37*(11), 1461-1475.

Dargent, J., Aunai, N., Lavraud, B., Toledo-Redondo, S., & Califano, F. (2020). Simulation of plasmaspheric plume impact on dayside magnetic reconnection. *Geophysical Research Letters*, *47*(4), e2019GL086546.

Desroche, M., Bagenal, F., Delamere, P. A., & Erkaev, N. (2013). Conditions at the magnetopause of saturn and implications for the solar wind interaction. *Journal of Geophysical Research: Space Physics*, *118*(6), 3087-3095.

Doss, C., Cassak, P., & Swisdak, M. (2016). Particle-in-cell simulation study of the scaling of asymmetric magnetic reconnection with in-plane flow shear. *Physics of Plasmas*, *23*(8), 082107.

Doss, C. E., Komar, C. M., Cassak, P. A., Wilder, F. D., Eriksson, S., & Drake, J. F. (2015). Asymmetric magnetic reconnection with a flow shear and applications to the magnetopause. *Journal of Geophysical Research: Space Physics*, *120*(9), 7748-7763.

Dunlop, M. W., Zhang, Q. H., Bogdanova, Y. V., Lockwood, M., Pu, Z., Hasegawa, H., … Liu, Z. X. (2011). Extended magnetic reconnection across the dayside magnetopause. *Physical Review Letters*, *107*(2), 025004.

Dusik, S., Granko, G., Safrankova, J., Nemecek, Z., & Jelinek, K. (2010). Imf cone angle control of the magnetopause location: Statistical study. *Geophysical Research Letters*, *37*(19).

Escoubet, C. P., Fehringer, M., & Goldstein, M. (2001). The cluster mission - introduction. *Annales Geophysicae*, *19*(10-12), 1197-1200.

Fairfield, D., Baumjohann, W., Paschmann, G., Lühr, H., & Sibeck, D. (1990). Upstream pressure variations associated with the bow shock and their effects on the magnetosphere. *Journal of Geophysical Research: Space Physics*, *95*(A4), 3773-3786.

Fairfield, D. H. (1971). Average and unusual locations of the earth's magnetopause and bow shock. *Journal of Geophysical Research*, *76*(28), 6700-6716.

Fear, R. C., Milan, S. E., Fazakerley, A. N., Fornaçon, K. H., Carr, C. M., & Dandouras, I. (2009). Simultaneous observations of flux transfer events by themis, cluster, double star, and superdarn: Acceleration of ftes. *Journal of Geophysical Research: Space Physics*, *114*(A10), n/a-n/a.

Fuselier, S., Petrinec, S., Sawyer, R., Mukherjee, J., & Masters, A. (2020). Suppression of magnetic reconnection at saturn's low-latitude magnetopause. *Journal of Geophysical Research: Space Physics*, *125*(5), e2020JA027895.

Fuselier, S. A., Burch, J. L., Mukherjee, J., Genestreti, K. J., Vines, S. K., Gomez, R., … Strangeway, R. J. (2017). Magnetospheric ion influence at the dayside magnetopause. *Journal of Geophysical Research: Space Physics*, *122*(8), 8617-8631.

Fuselier, S. A., Haaland, S., Tenfjord, P., Paschmann, G., Toledo-Redondo, S., Malaspina, D., … Giles, B. L. (2021). High-density magnetospheric he+ at the dayside magnetopause and its effect on magnetic reconnection. *Journal of Geophysical Research: Space Physics*, *126*(1), 2020JA028722.

Fuselier, S. A., Mukherjee, J., Denton, M. H., Petrinec, S. M., Trattner, K. J., Toledo-Redondo, S., … Glocer, A. (2019). High-density o+ in earth's outer magnetosphere and its effect on dayside magnetopause magnetic reconnection. *Journal of Geophysical Research: Space Physics*, *124*(12), 10257-10269.

Fuselier, S. A., Trattner, K. J., Petrinec, S. M., Denton, M. H., Toledo-Redondo, S., André, M., … Strangeway, R. J. (2019). Mass loading the earth's dayside magnetopause boundary layer and its effect on magnetic reconnection. *Geophysical Research Letters*, *46*(12), 6204-6213.

Genestreti, K. J., Varsani, A., Burch, J. L., Cassak, P. A., Torbert, R. B., Nakamura, R., … Baumjohann, W. (2018). Mms observation of asymmetric reconnection supported by 3-d electron pressure divergence. *Journal of Geophysical*

Research: Space Physics.

Gosling, J. T., Thomsen, M. F., Bame, S. J., Onsager, T. G., & Russell, C. T. (1990). The electron edge of low latitude boundary layer during accelerated flow events. *Geophysical research letters*, *17*(11), 1833-1836.

Kitamura, N., Hasegawa, H., Saito, Y., Shinohara, I., Yokota, S., Nagai, T., ... Burch, J. L. (2016). Shift of the magnetopause reconnection line to the winter hemisphere under southward imf conditions: Geotail and mms observations. *Geophysical Research Letters*, *43*(11), 5581-5588.

La Belle-Hamer, A., Otto, A., & Lee, L. (1995). Magnetic reconnection in the presence of sheared flow and density asymmetry: Applications to the earth's magnetopause. *Journal of Geophysical Research: Space Physics*, *100*(A7), 11875-11889.

Lavraud, B., & Borovsky, J. E. (2008). Altered solar wind-magnetosphere interaction at low mach numbers: Coronal mass ejections. *Journal of Geophysical Research: Space Physics*, *113*(A9).

Le, G., & Russell, C. (1994). The thickness and structure of high beta magnetopause current layer. *Geophysical research letters*, *21*(23), 2451-2454.

Lin, R. L., Zhang, X. X., Liu, S. Q., Wang, Y. L., & Gong, J. C. (2010). A three-dimensional asymmetric magnetopause model. *Journal of Geophysical Research: Space Physics*, *115*(A4), n/a-n/a.

Lu, J., Liu, Z., Kabin, K., Jing, H., Zhao, M., & Wang, Y. (2013). The imf dependence of the magnetopause from global mhd simulations. *Journal of Geophysical Research: Space Physics*, *118*(6), 3113-3125.

Lu, J., Liu, Z., Kabin, K., Zhao, M., Liu, D., Zhou, Q., & Xiao, Y. (2011). Three dimensional shape of the magnetopause: Global mhd results. *Journal of Geophysical Research: Space Physics*, *116*(A9).

Marchaudon, A., Owen, C., Bosqued, J.-M., Fear, R., Fazakerley, A., Dunlop, M., ... Lindqvist, P.-A. (2005). Simultaneous double star and cluster ftes observations on the dawnside flank of the magnetosphere. In *Annales geophysicae* (Vol. 23, p. 2877-2887). Copernicus GmbH.

Merka, J., Szabo, A., Šafránková, J., & Němeček, Z. (2003). Earth's bow shock and magnetopause in the case of a field-aligned upstream flow: Observation and model comparison. *Journal of Geophysical Research: Space Physics*, *108*(A7).

Palmroth, M., Janhunen, P., Pulkkinen, T., & Peterson, W. (2001). Cusp and magnetopause locations in global mhd simulation. *Journal of Geophysical Research: Space Physics*, *106*(A12), 29435-29450.

Park, J., Shue, J., Kim, K., Pi, G., Němeček, Z., & Šafránková, J. (2016). Global expansion of the dayside magnetopause for long-duration radial imf events: Statistical study on goes observations. *Journal of Geophysical Research: Space Physics*, *121*(7), 6480-6492.

Petrinec, S., & Russell, C. (1996). Near-earth magnetotail shape and size as determined from the magnetopause flaring angle. *Journal of Geophysical Research: Space Physics*, *101*(A1), 137-152.

Phan, T., Hasegawa, H., Fujimoto, M., Oieroset, M., Mukai, T., Lin, R., & Paterson, W. (2006). Simultaneous geotail and wind observations of reconnection at the subsolar and tail flank magnetopause. *Geophysical research letters*, *33*(9).

Phan, T., Kistler, L., Klecker, B., Haerendel, G., Paschmann, G., Sonnerup, B. O., ... DiLellis, A. (2000). Extended magnetic reconnection at the earth's magnetopause from detection of bi-directional jets. *Nature*, *404*(6780), 848-850.

Phan, T., Paschmann, G., Gosling, J., Oieroset, M., Fujimoto, M., Drake, J., & Angelopoulos, V. (2013). The dependence of magnetic reconnection on plasma beta and magnetic shear: Evidence from magnetopause observations. *Geophysical Research Letters*, *40*(1), 11-16.

Pi, G., Shue, J., Chao, J., Němeček, Z., Šafránková, J., & Lin, C. (2014). A reexamination of long-duration radial imf events. *Journal of Geophysical Research:*

Space Physics, *119*(9), 7005-7011.
Pollock, C., Moore, T., Jacques, A., Burch, J., Gliese, U., Saito, Y., … Zeuch, M. (2016). Fast plasma investigation for magnetospheric multiscale. *Space Science Reviews*, *199*(1-4), 331-406.
Reme, H., Aoustin, C., Bosqued, J., Dandouras, I., Lavraud, B., Sauvaud, J., … Coeur-Joly, O. (2001). First multispacecraft ion measurements in and near the earth's magnetosphere with the identical cluster ion spectrometry (cis) experiment. In *Annales geophysicae* (Vol. 19, p. 1303-1354). Copernicus GmbH.
Russell, C. T., Anderson, B. J., Baumjohann, W., Bromund, K. R., Dearborn, D., Fischer, D., … Richter, I. (2014). The magnetospheric multiscale magnetometers. *Space Science Reviews*, *199*(1-4), 189-256.
Safrankova, J., Nemecek, Z., Dusik, S., Prech, L., Sibeck, D., & Borodkova, N. (2002). The magnetopause shape and location: A comparison of the interball and geotail observations with models. In *Annales geophysicae* (Vol. 20, p. 301-309). Copernicus GmbH.
Samsonov, A. A., Gordeev, E., Tsyganenko, N. A., Šafránková, J., Němeček, Z., Šimůnek, J., … Raeder, J. (2016). Do we know the actual magnetopause position for typical solar wind conditions? *Journal of Geophysical Research: Space Physics*, *121*(7), 6493-6508.
Samsonov, A. A., Němeček, Z., Šafránková, J., & Jelínek, K. (2012). Why does the subsolar magnetopause move sunward for radial interplanetary magnetic field? *Journal of Geophysical Research: Space Physics*, *117*(A5), n/a-n/a.
Sawyer, R., Fuselier, S., Mukherjee, J., & Petrinec, S. (2019). An investigation of flow shear and diamagnetic drift effects on magnetic reconnection at saturn's dawnside magnetopause. *Journal of Geophysical Research: Space Physics*, *124*(11), 8457-8473.
Shue, J., Song, P., Russell, C., Steinberg, J., Chao, J., Zastenker, G., … Detman, T. (1998). Magnetopause location under extreme solar wind conditions. *Journal of Geophysical Research: Space Physics*, *103*(A8), 17691-17700.
Sibeck, D. G., Lopez, R., & Roelof, E. C. (1991). Solar wind control of the magnetopause shape, location, and motion. *Journal of Geophysical Research: Space Physics*, *96*(A4), 5489-5495.
Suvorova, A., & Dmitriev, A. (2015). Magnetopause inflation under radial imf: Comparison of models. *Earth and Space Science*, *2*(4), 107-114.
Suvorova, A., & Dmitriev, A. (2016). On magnetopause inflation under radial imf. *Advances in Space Research*, *58*(2), 249-256.
Suvorova, A., Shue, J., Dmitriev, A., Sibeck, D., McFadden, J., Hasegawa, H., … Němeček, Z. (2010). Magnetopause expansions for quasi-radial interplanetary magnetic field: Themis and geotail observations. *Journal of Geophysical Research: Space Physics*, *115*(A10).
Swisdak, M., Opher, M., Drake, J., & Bibi, F. A. (2010). The vector direction of the interstellar magnetic field outside the heliosphere. *The Astrophysical Journal*, *710*(2), 1769.
Swisdak, M., Rogers, B., Drake, J., & Shay, M. (2003). Diamagnetic suppression of component magnetic reconnection at the magnetopause. *Journal of Geophysical Research: Space Physics*, *108*(A5).
Trattner, K., Mulcock, J., Petrinec, S., & Fuselier, S. (2007). Probing the boundary between antiparallel and component reconnection during southward interplanetary magnetic field conditions. *Journal of Geophysical Research: Space Physics*, *112*(A8).
Vernisse, Y., Lavraud, B., Faganello, M., Fadanelli, S., Sisti, M., Califano, F., … Pollock, C. (2020). Latitudinal dependence of the kelvin-helmholtz instability and beta dependence of vortex-induced high-guide field magnetic reconnection. *Journal of Geophysical Research: Space Physics*, *125*(5), e2019JA027333.
Vines, S. K., Fuselier, S. A., Trattner, K. J., Burch, J. L., Allen, R. C., Petrinec,

S. M., ... Russell, C. T. (2017). Magnetospheric ion evolution across the low-latitude boundary layer separatrix. *Journal of Geophysical Research: Space Physics*, *122*(10), 10,247-10,262.

Walsh, B. M., Komar, C. M., & Pfau-Kempf, Y. (2017). Spacecraft measurements constraining the spatial extent of a magnetopause reconnection x line. *Geophysical Research Letters*, *44*(7), 3038-3046.

Walsh, B. M., Sibeck, D. G., Nishimura, Y., & Angelopoulos, V. (2013). Statistical analysis of the plasmaspheric plume at the magnetopause. *Journal of Geophysical Research: Space Physics*, *118*(8), 4844-4851.

Wang, Y., Sibeck, D., Merka, J., Boardsen, S., Karimabadi, H., Sipes, T., ... Lin, R. (2013). A new three-dimensional magnetopause model with a support vector regression machine and a large database of multiple spacecraft observations. *Journal of Geophysical Research: Space Physics*, *118*(5), 2173-2184.

Wiltberger, M., Lopez, R., & Lyon, J. (2003). Magnetopause erosion: A global view from mhd simulation. *Journal of Geophysical Research: Space Physics*, *108*(A6).

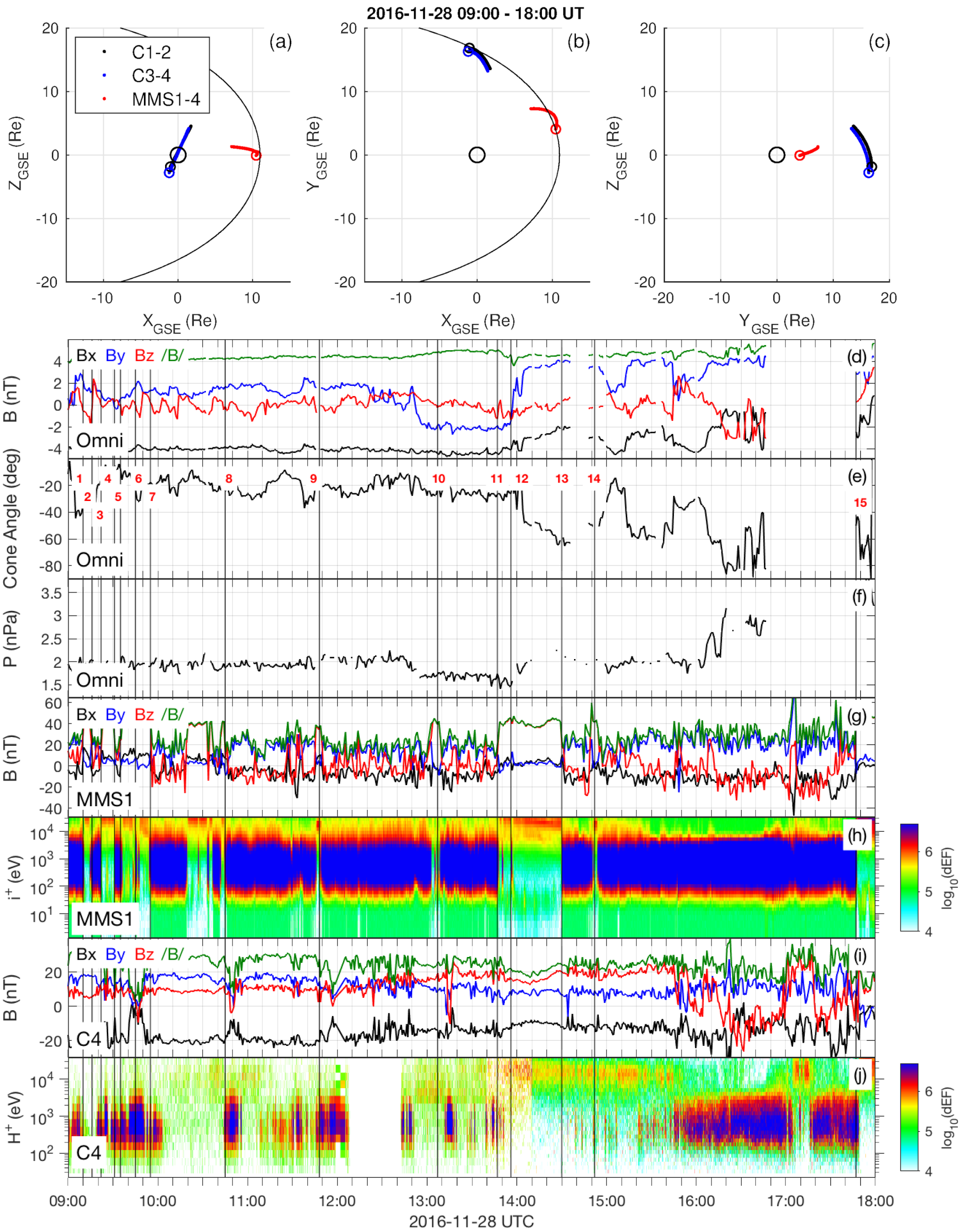

Figure 1. Overview of the 2016-11-28 MMS - Cluster magnetopause conjunction. (a) Spacecraft orbits, XZ GSE plane. (b) Spacecraft orbits, XY GSE plane. (c) Spacecraft orbits, YZ GSE plane. (d) Solar wind magnetic field in GSE coordinates (omni database). (e) IMF cone angle (omni database). (f) Solar wind dynamic pressure (omni database). (g) MMS magnetic field in GSE coordinates. (h) MMS FPI ion spectrogram in differential Energy Flux units (dEF), keV/(cm^2 s sr keV). (i) C4 magnetic field in GSE coordinates. (j) C4 CODIF proton spectrogram in differential Energy Flux units (dEF), keV/(cm^2 s sr keV). Black vertical lines correspond to the occurrence times of events 1-15 in Table 1.

Table 1. Simultaneous (∼5 min) MMS and Cluster Magnetopause crossings

	MMS 1-4			Cluster 1-2			Cluster 3-4		
ID	Time (UT)	Position[a] (GSE R_E)	B rotation[b]	Time (UT)	Position[a] (GSE R_E)	B rotation[b]	Time (UT)	Position[a] (GSE R_E)	B rotation[b]
1	09:10	10.5, 4.2, 0.0	full S-M	09:13	-1.0, 16.8, -1.7	full S-M	-	-	-
2	09:16	10.5, 4.2, 0.0	full M-S	09:20	-1.0, 16.8, -1.7	full M-S	09:20	-1.1, 16.3, -2.6	partial M-S-M
3	09:22	10.5, 4.3, 0.0	full S-M	-	-	-	09:25	-1.1, 16.3, -2.5	full M-S-M
4	09:31	10.6, 4.4, 0.0	full M-S	-	-	-	09:31	-1.0, 16.3, -2.4	partial M-S-M
5	09:35	10.6, 4.4, 0.0	full S-M	-	-	-	09:41	-1.0, 16.3, -2.4	full M-S
6	09:45	10.6, 4.5, 0.1	full M-S-M	-	-	-	09:51	-1.0, 16.3, -2.2	full S-M
7	09:55	10.6, 4.6, 0.1	full M-S	-	-	-	09:53	-0.9, 16.3, -2.1	partial M-S-M
8	10:45	10.6, 5.2, 0.2	full M-S	10:43	-0.5, 16.7, -0.6	full M-S	10:47	-0.7, 16.2, -1.4	full M-S
9	11:48	10.5, 5.7, 0.4	full S-M-S	-	-	-	11:48	-0.4, 16.1, -0.6	full M-S
10	13:07	10.2, 6.3, 0.6	full S-M-S	13:12	0.3, 16.1, 1.1	full M-S?	13:13	0.0, 15.7, 0.4	full M-S-M
11	13:47	9.9, 6.6, 0.8	full S-M	13:50	0.5, 15.9, 1.6	?	13:45	0.2, 15.5, 1.0	full M-S-M
12	13:56	9.9, 6.6, 0.8	partial M-S-M	13:56	0.5, 15.8, 1.7	partial M-S-M	13:56	0.3, 15.5, 1.1	partial M-S-M
13	14:30	9.6, 6.8, 0.9	full M-S	14:34	0.7, 15.6, 2.1	full M-S	14:34	0.4, 15.2, 1.5	partial M-S-M
14	14:52	9.4, 6.9, 0.9	full S-M-S	14:52	0.8, 15.4, 2.4	full S-M-S	14:52	0.5, 15.1, 1.8	multiple partial
15	17:47	7.4, 7.3, 1.3	full S-M	17:50	1.7, 13.8, 4.4	full S-M	17:48	1.4, 13.4, 4.0	full S-M

[a]Position corresponds to mean values during a 50 s interval centered at the reference time.
[b]Type of crossing, S stands for magnetosheath and M stands for Magnetosphere.

Table 2. Distance to magnetopause models

	SW parameters					Model deviation (subsolar)				Model deviation (flank)			
ID	P_d (nPa)	P_m (nPa)	Φ ($^\circ$)	B_z (nT)	B_x/B	S98 (R_E)	S98$_c$ (R_E)	L10 (R_E)	L10$_c$ (R_E)	S98 (R_E)	S98$_c$ (R_E)	L10 (R_E)	L10$_c$ (R_E)
1	1,8	0,0	-24,8	-0,6	-0,8	-0,7	-0,3	-0,5	0,1	-0,2	0,3	0,4	0,5
2	1,9	0,0	-24,5	-1,1	-0,9	-0,8	-0,4	-0,7	-0,1	-0,3	0,3	-0,5	0,3
3	1,8	0,0	-24,3	0,2	-1,0	-0,7	-0,2	-0,4	0,2	-0,2	0,4	0,2	0,7
4	1,9	0,0	-23,9	0,3	-1,0	-0,8	-0,4	-0,5	-0,2	-0,3	0,3	0,3	-0,5
5	1,8	0,0	-23,8	0,2	-1,0	-0,8	-0,3	-0,5	0,1	-0,2	0,3	0,2	0,6
6	1,8	0,0	-23,3	0,1	-0,9	-0,8	-0,4	-0,5	0,1	-0,2	0,4	-0,2	0,6
7	1,8	0,0	-22,9	0,5	-0,9	-0,9	-0,4	-0,6	0,1	-0,2	0,3	-0,2	0,5
8	1,8	0,0	-20,9	-0,1	-0,9	-1,0	-0,6	-0,7	-0,2	-0,1	0,4	-0,3	0,6
9	1,9	0,0	-18,3	0,1	-0,9	-1,2	-0,8	-1,0	-0,4	-0,3	0,2	-0,4	0,4
10	1,6	0,0	-15,5	-0,2	-0,9	-0,9	-0,5	-0,6	-0,1	0,1	0,7	-0,1	0,8
11	1,6	0,0	-14,3	-1,2	-0,9	-0,8	-0,4	-0,7	-0,2	0,2	0,8	-0,3	0,7
12	1,4	0,0	-14,1	-1,3	-0,9	-0,5	-0,1	-0,4	0,2	0,5	1,1	0,4	1,2
13	2,0	0,0	-13,3	-0,5	-0,6	-1,0	-0,7	-0,8	-0,5	-0,1	0,2	0,4	0,1
14	2,0	0,0	-12,8	0,7	-0,5	-0,8	-0,5	-0,7	-0,3	-0,1	0,2	-0,3	-0,2
15	3,2	0,0	-12,3	0,3	-0,6	0,1	0,3	-0,1	0,3	-0,3	-0,1	-0,8	-0,5

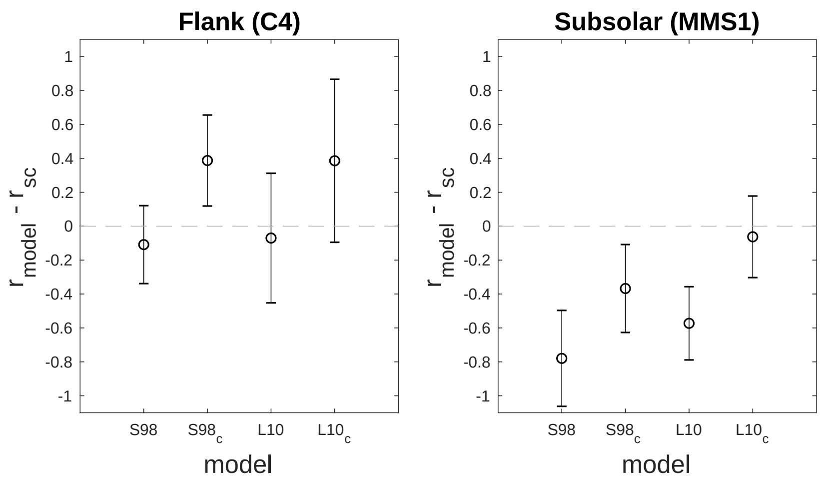

Figure 2. (left) Distance between the mean observed magnetopause position in the flank (r_{sc}), averaged over the 15 events of Table 1, and the MP model predictions (r_{model}). (right) Distance between the mean observed magnetopause position in the subsolar region (r_{sc}), averaged over the 15 events of Table 1, and the MP model predictions (r_{model}). Error bars correspond to one standard deviation.

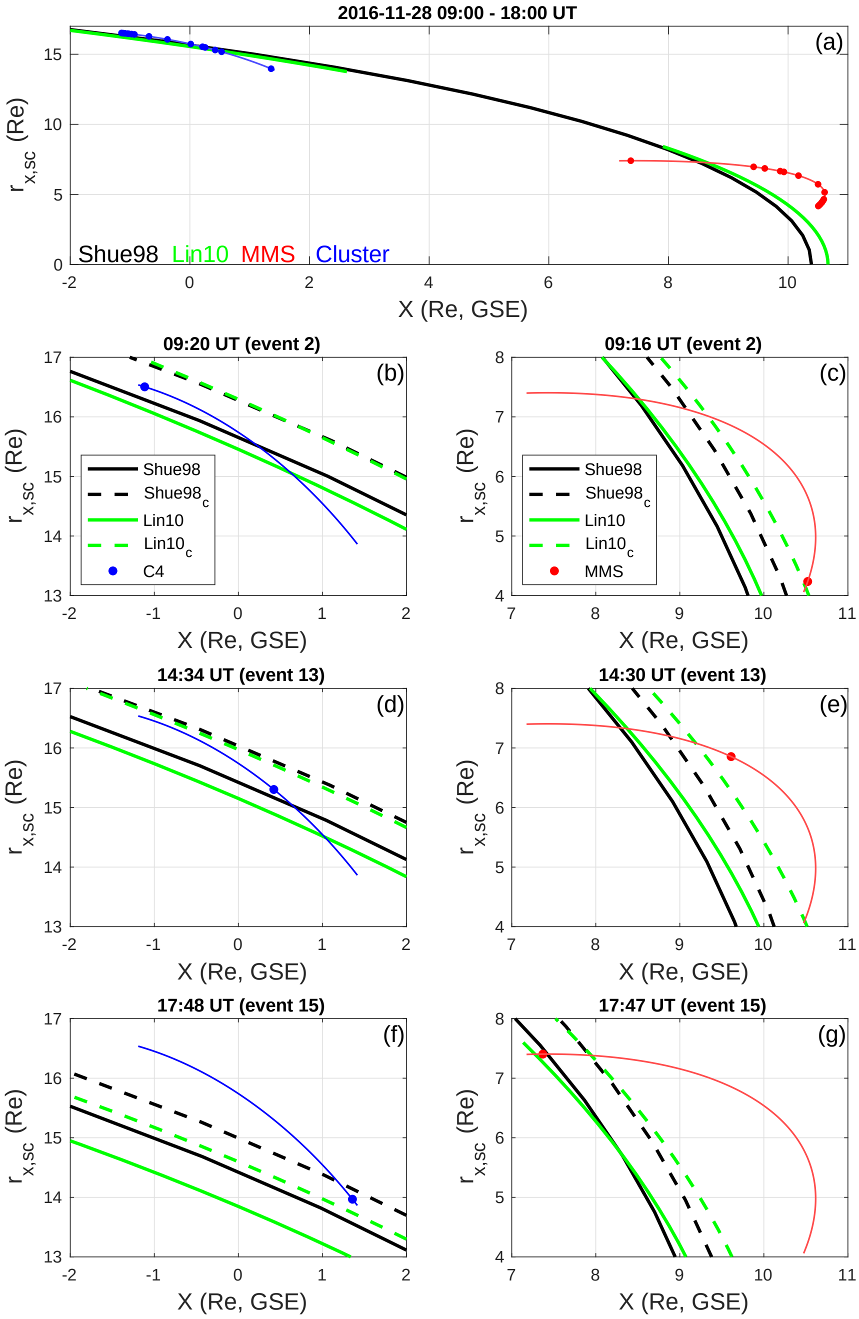

Figure 3. Magnetopause models estimation during the MMS - Cluster conjunction (2016-11-28 09:00 - 18:00 UT). (a) C4 (blue) and MMS (red) orbits, the spacecraft position at the times indicated in Table 1 are marked using circles. (Black) Reference S98 model and (green) reference L10 model. (b) Detail of the C4 position for event 2 in Table1. (Solid) S98 and L10 models for nominal solar wind conditions and (dashed) for corrected solar wind conditions (Samsonov et al., 2012). (c) Detail of the MMS position for event 2 in Table1. (Solid) S98 and L10 models for nominal solar wind conditions and (dashed) for corrected solar wind conditions (Samsonov et al., 2012). (d) Same as (b) for event 13 in Table 1. (e) Same as (c) for event 13 in Table 1. (f) Same as (b) for event 15 in Table 1. (g) Same as (c) for event 15 in Table 1.

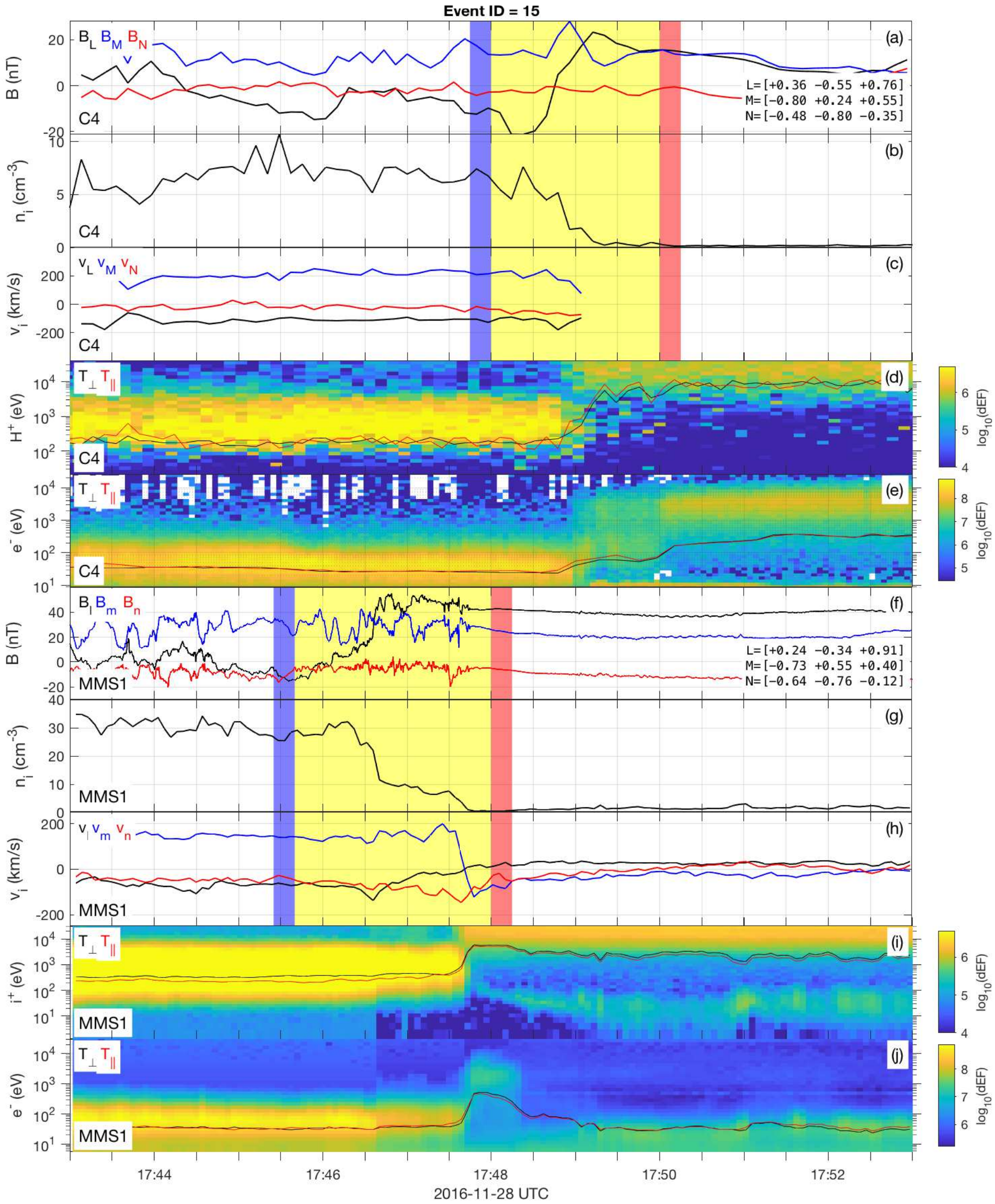

Figure 4. MMS and Cluster simultaneous observations of the magnetopause during event 15 (see Table 1). The yellow-shaded regions mark the time interval used to apply MVA to the current sheet crossing and obtain the LMN coordinate system for each spacecraft. Blue-shaded and red-shaded regions mark the intervals used as reference for the asymptotic conditions of the magnetosheath and the magnetosphere, respectively. (a) C4 magnetic field in LMN coordinates. (b) C4 ion number density. (c) C4 ion velocity in LMN coordinates. (d) (color) C4 CODIF proton spectrogram in differential Energy Flux units (dEF), keV/(cm^2 s sr keV), (black) perpendicular proton temperature, (red) parallel proton temperature. (e) (color) C4 PEACE electron spectrogram in differential Energy Flux units (dEF), keV/(cm^2 s sr keV), (black) perpendicular electron temperature, (red) parallel electron temperature. (f) MMS magnetic field in LMN coordinates. (g) MMS ion number density. (h) MMS ion velocity in LMN coordinates. (i) (color) MMS FPI ion spectrogram in differential Energy Flux units (dEF), keV/(cm^2 s sr keV), (black) perpendicular ion temperature, (red) parallel ion temperature. (j) (color) MMS FPI electron spectrogram in differential Energy Flux units (dEF), keV/(cm^2 s sr keV), (black) perpendicular electron temperature, (red) parallel electron temperature.

Table 3. Magnetic reconnection assessment at dusk flank (C4) and subsolar region (MMS)

ID	SC	L (GSE)	v_A[a] (km/s)	$v_{s,L}$[b] (km/s)	$(E/E_0)^c_{asym}$	Swisdak[d] prediction	Observed jet	e^- only LLBL
3	C4 MMS	-0.51 +0.27 -0.82 +0.50 -0.28 +0.82	338 124	225 16	0.80 1.00	? suppress	no no	? yes
5	C4 MMS	-0.82 +0.54 -0.16 +0.11 +0.48 +0.87	146 249	262 15	0.71 1.00	suppress suppress	no ?	? yes
6	C4 MMS	-0.78 +0.60 +0.16 +0.50 -0.29 +0.82	221 188	248 1	0.95 1.00	suppress ?	no yes	no yes
8	C4 MMS	-0.59 +0.50 +0.64 +0.38 -0.45 +0.81	159 187	223 51	0.96 1.00	suppress ?	no ?	no yes
10	C4 MMS	+0.18 -0.41 +0.89 -0.05 -0.36 +0.93	187 169	163 100	0.95 0.98	? ?	? yes	? yes
11	C4 MMS	-0.62 +0.33 +0.71 +0.33 -0.53 +0.78	192 177	150 71	0.83 0.99	suppress ?	? yes	yes yes
15	C4 MMS	+0.36 -0.55 +0.76 +0.24 -0.34 +0.91	228 223	116 86	0.98 1.00	allow ?	? ?	yes yes

See Table S1 of the supplemental material for additional information of the computed values.
[a] Hybrid Alfvén velocity (Cassak & Shay, 2007).
[b] Shear flow speed parallel to the outflow (L) direction.
[c] Expected reduction in reconnection rate due to shear flows, see Equation 3.
[d] Diamagnetic drift of the X line, see Equation 4.

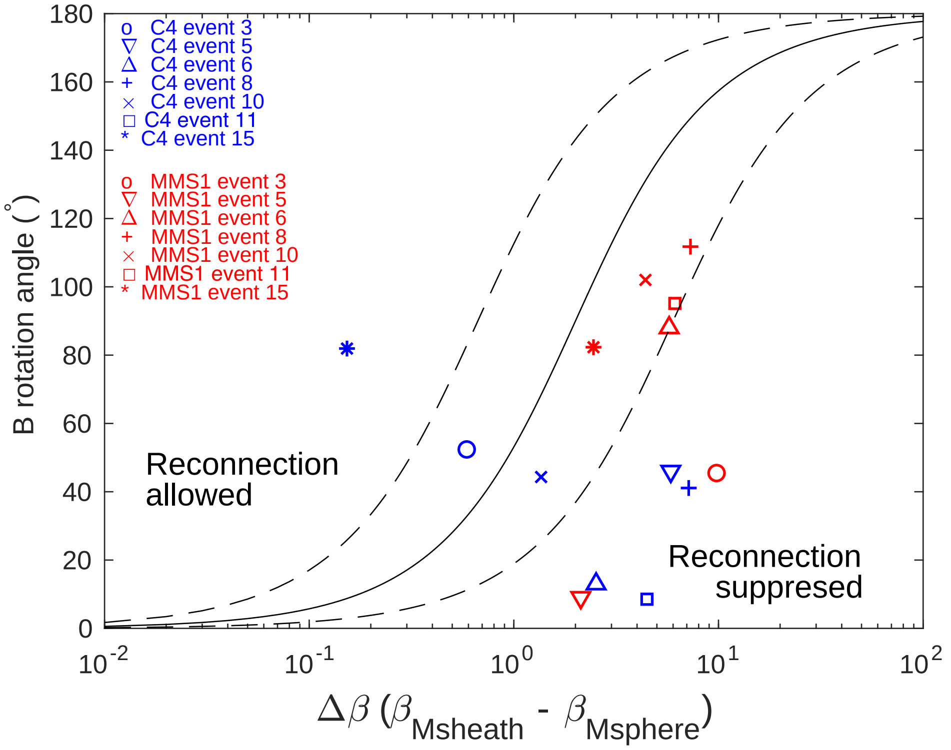

Figure 5. Local test of the diamagnetic drift reconnection suppression (Swisdak et al., 2003). Magnetic field clock angle in the LM plane versus corresponding change in plasma β across the magnetopause current sheet ($\Delta\beta$), for all the crossings of Table 3. The solid line indicates $L/d_i = 1$, and the dashed lines indicate $L/d_i = 1/3$ and 3, see Equation 4.

Figure 1.

2016-11-28 09:00 - 18:00 UT
C1-2
C3-4
MMS1-4
(a)
(b)
(c)
Z_{GSE} (Re)
Y_{GSE} (Re)
X_{GSE} (Re)
Y_{GSE} (Re)
Bx By Bz /B/
B (nT)
Omni
(d)
Cone Angle (deg)
(e)
1 2 3 4 5 6 7 8 9 10 11 12 13 14 15
P (nPa)
(f)
MMS1
(g)
i^+ (eV)
(h)
log_{10}(dEF)
C4
(i)
H^+ (eV)
(j)
09:00 10:00 11:00 12:00 13:00 14:00 15:00 16:00 17:00 18:00
2016-11-28 UTC

Figure 2.

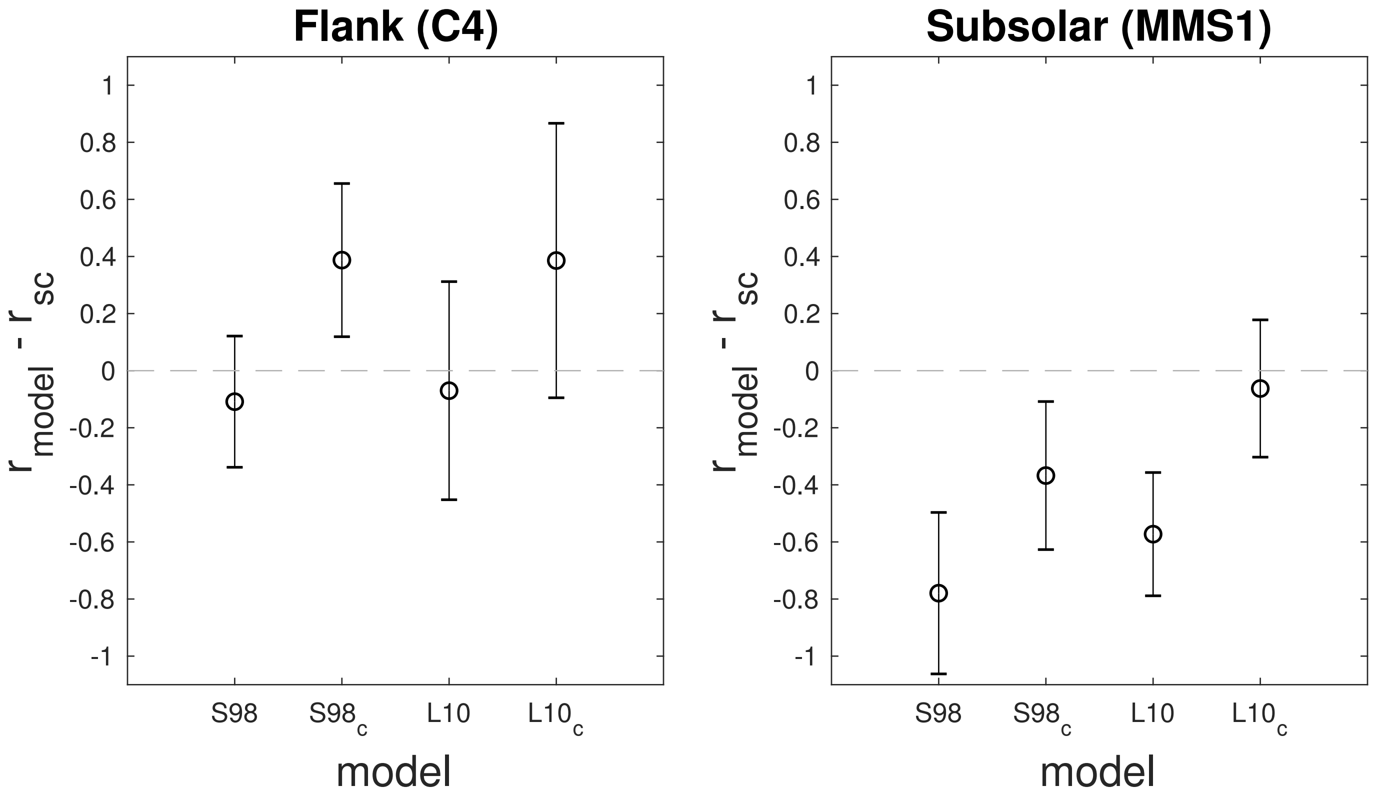

Flank (C4)
Subsolar (MMS1)
$r_{model} - r_{sc}$
1
0.8
0.6
0.4
0.2
0
-0.2
-0.4
-0.6
-0.8
-1
S98
$S98_c$
L10
$L10_c$
model

Figure 3.

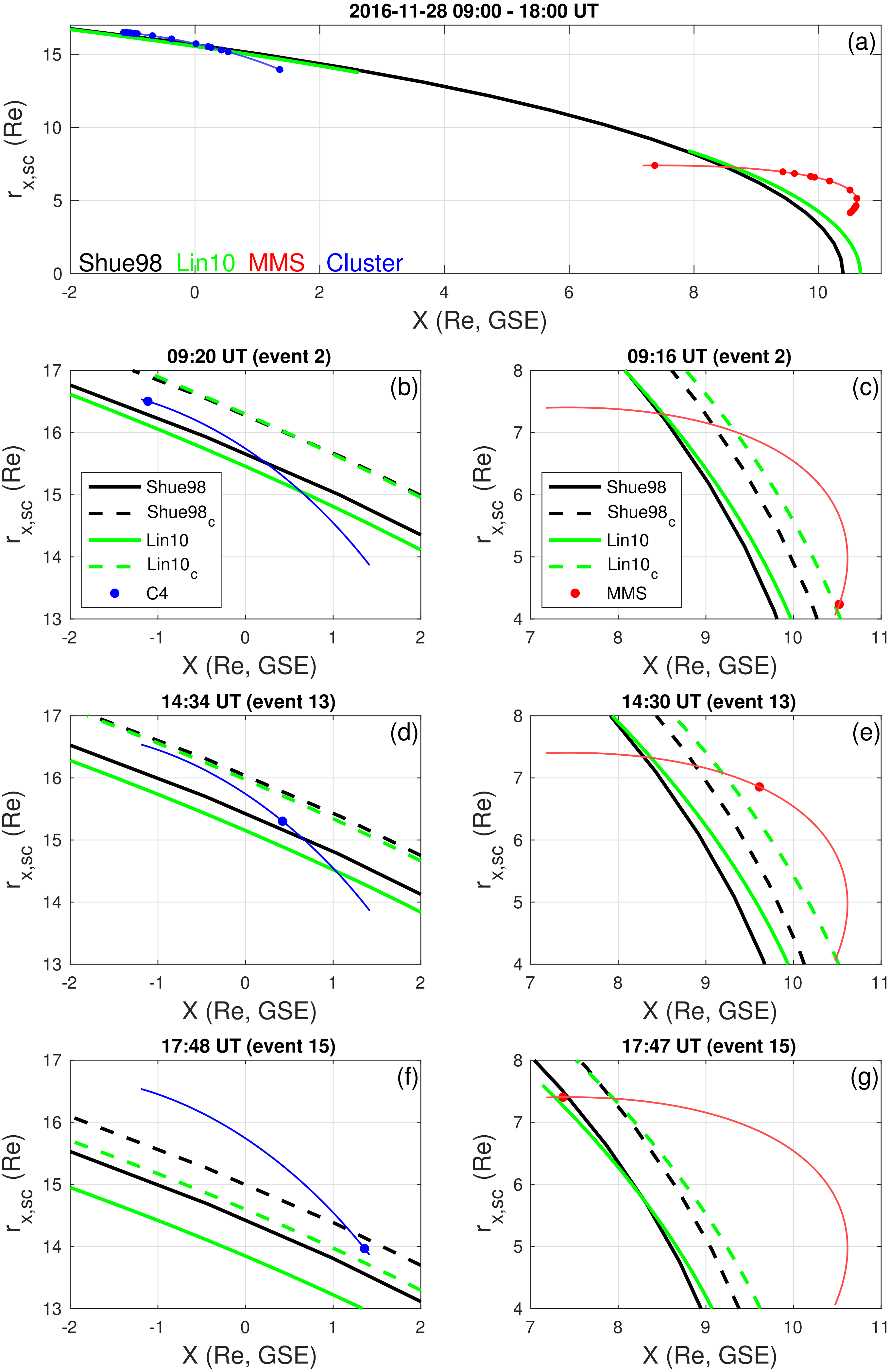

2016-11-28 09:00 - 18:00 UT
(a)
Shue98 Lin10 MMS Cluster
$r_{x,sc}$ (Re)
X (Re, GSE)
09:20 UT (event 2)
(b)
Shue98
$Shue98_c$
Lin10
$Lin10_c$
C4
09:16 UT (event 2)
(c)
MMS
14:34 UT (event 13)
(d)
14:30 UT (event 13)
(e)
17:48 UT (event 15)
(f)
17:47 UT (event 15)
(g)

Figure 4.

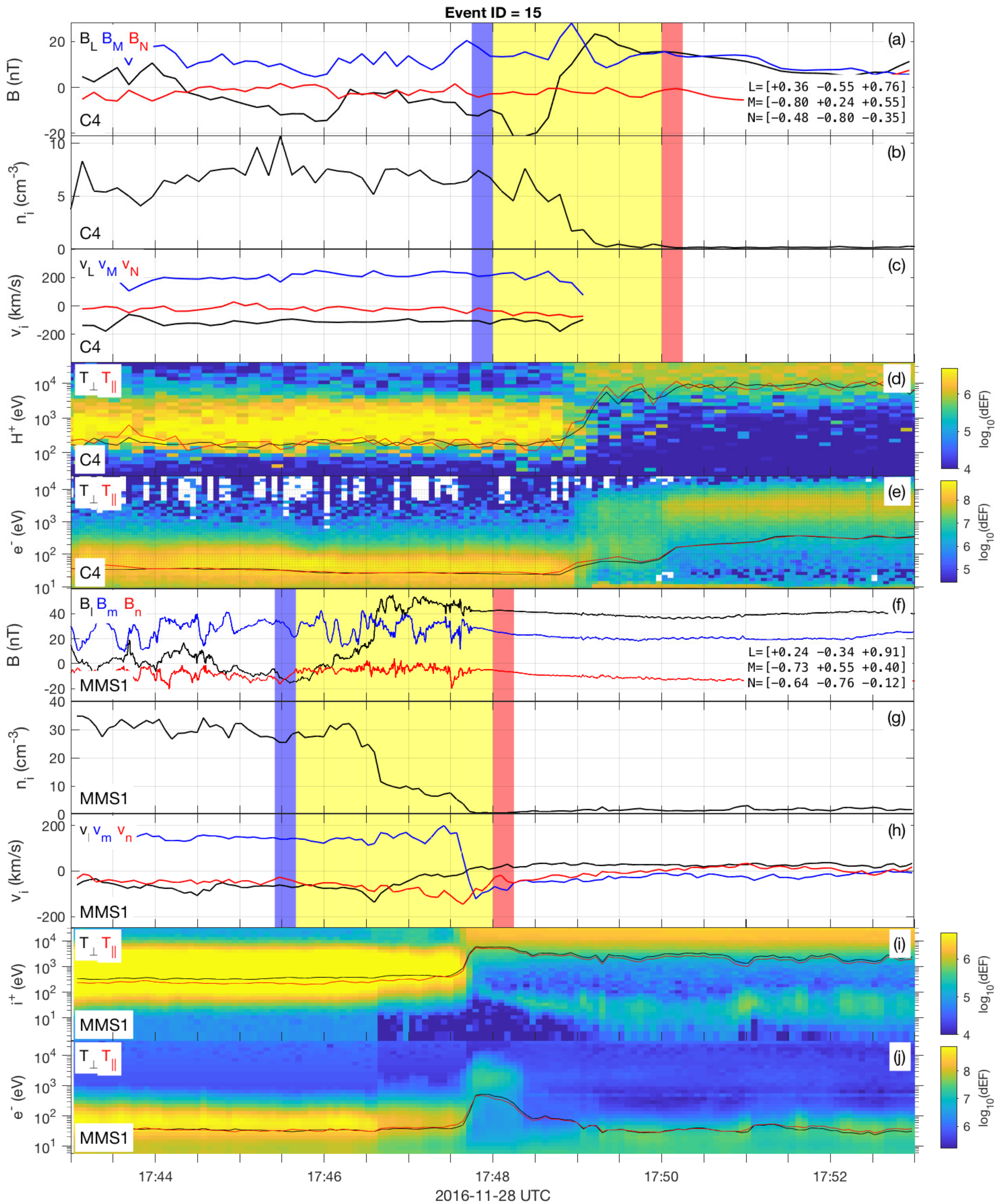

Event ID = 15
B (nT)
C4
L=[+0.36 -0.55 +0.76]
M=[-0.80 +0.24 +0.55]
N=[-0.48 -0.80 -0.35]
n_i (cm^-3)
v_i (km/s)
H+ (eV)
e- (eV)
log10(dEF)
MMS1
L=[+0.24 -0.34 +0.91]
M=[-0.73 +0.55 +0.40]
N=[-0.64 -0.76 -0.12]
i+ (eV)
17:44
17:46
17:48
17:50
17:52
2016-11-28 UTC

Figure 5.

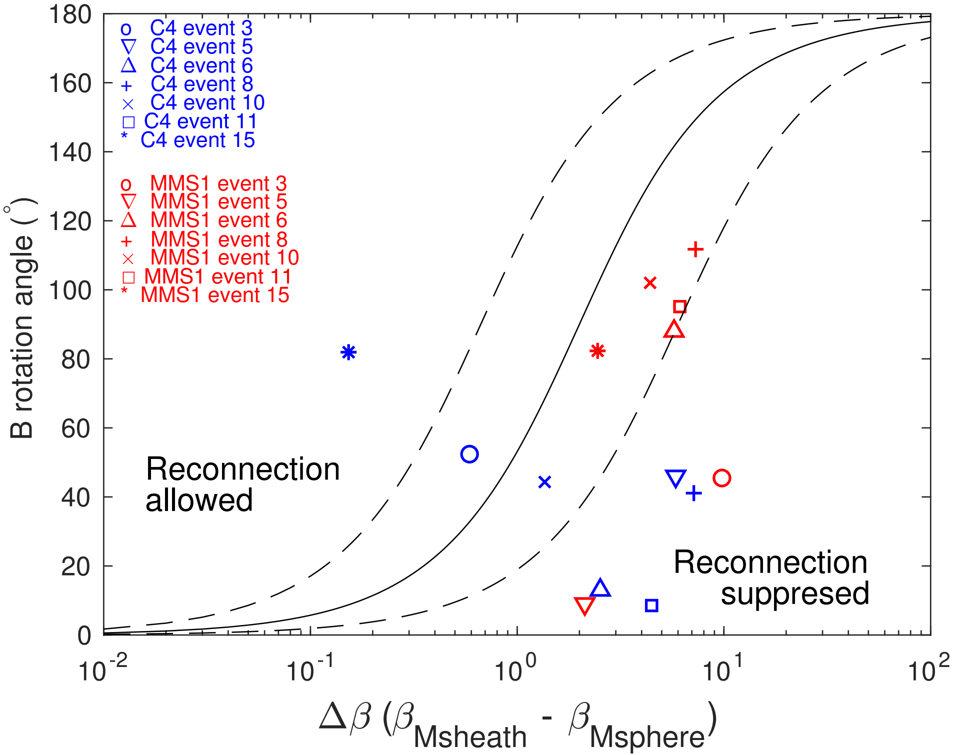

o C4 event 3
∇ C4 event 5
Δ C4 event 6
+ C4 event 8
× C4 event 10
□ C4 event 11
* C4 event 15
o MMS1 event 3
∇ MMS1 event 5
Δ MMS1 event 6
+ MMS1 event 8
× MMS1 event 10
□ MMS1 event 11
* MMS1 event 15
Reconnection allowed
Reconnection suppresed
B rotation angle (°)
0
20
40
60
80
100
120
140
160
180
10^{-2}
10^{-1}
10^{0}
10^{1}
10^{2}
$\Delta\beta$ ($\beta_{Msheath}$ - $\beta_{Msphere}$)

Supporting Information for "Solar wind - magnetosphere coupling during radial IMF conditions: simultaneous multi-point observations"

S. Toledo-Redondo [1,2], K.-J. Hwang [3], C. P. Escoubet [4], B. Lavraud [5,2], J. Fornieles [6], N. Aunai [7], R. C. Fear [8], J. Dargent [9], H. Fu [10], S. A. Fuselier [3,11], K. J. Genestreti [12], Yu. V. Khotyaintsev [13], Wy. Li [14], C. Norgren [15], and T. D. Phan [16]

[1]Department of Electromagnetism and Electronics, University of Murcia, Murcia, Spain.
[2]Institut de Recherche en Astrophysique et Planétologie, Université de Toulouse, CNRS, UPS, CNES, Toulouse, France.
[3]Southwest Research Institute, San Antonio, Texas, USA.
[4]ESA, European Space Research and Technology Centre, Noordwijk, Netherlands.
[5]Laboratoire d'Astrophysique de Bordeaux, Univ. Bordeaux, CNRS, B18N, allée Geoffroy Saint-Hilaire, 33615 Pessac, France
[6]Department of Electromagnetism and Matter Physics, University of Granada, Granada, Spain.
[7]UMR7648 Laboratoire de physique des plasmas (LPP), Palaiseau, France.
[8]School of Physics and Astronomy, University of Southampton, Southampton, United Kingdom.
[9]Institut für Theoretische Physik, Ruhr-Universität Bochum, Bochum, Germany.
[10]School of Space and Environment, Beihang University, Beijing, China.
[11]Department of Physics and Astronomy, University of Texas at San Antonio, San Antonio, TX, USA.
[12]Southwest Research Institute, Durham, NH, USA.
[13]Swedish institute of Space Physics, Uppsala, Sweden.
[14]State Key Laboratory of Space Weather, National Space Science Center, Chinese Academy of Sciences, Beijing, 100190, China.
[15]University of Bergen, Bergen, Norway.
[16]SSL, University of California, Berkeley, CA 94720, USA.

Figures S1 - S6 show the Cluster 4 (dusk flank) and MMS1 (subsolar region) magnetopause crossings for events with ID 3, 5, 6, 8, 10 and 11 (see Table 1 of the main article). Panels a-e correspond to Cluster (C4) observations, and panels f-j correspond to MMS observations of the same variables, namely magnetic field, ion density, ion velocity, and ion spectrogram. All vectors are provided in local LMN coordinates, obtained from applying MVA to the **B** field in the yellow-shaded regions. The LMN coordinates are specified in panels a and f, for C4 and MMS1, respectively. The blue-shaded regions correspond to the reference time interval for inferring magnetosheath quantities, and the red-shaded regions correspond to the reference time interval for inferring magnetospheric quantities. Ion velocities estimated by CIS-CODIF on C4 are not reliable in the magnetosphere due to the low counts, and have been masked in panel c. We assume a negligible flank magnetosphere bulk velocity, compared to flank magnetosheath bulk velocity.

Table S1 complements Table 1 of the main article. It provides, for each spacecraft crossing, the local L and N directions of the magnetopause current sheet, the average B_L and n values in the magnetosphere and magnetosheath reference intervals, the hybrid Alfvén velocity (Cassak & Shay, 2007), the shear flow velocity in the L direction at the magnetopause, the variation of plasma β, and the **B** clock angle in the local LM plane.

References

Cassak, P. A., & Shay, M. A. (2007). Scaling of asymmetric magnetic reconnection: General theory and collisional simulations. *Physics of Plasmas*, *14*(10).

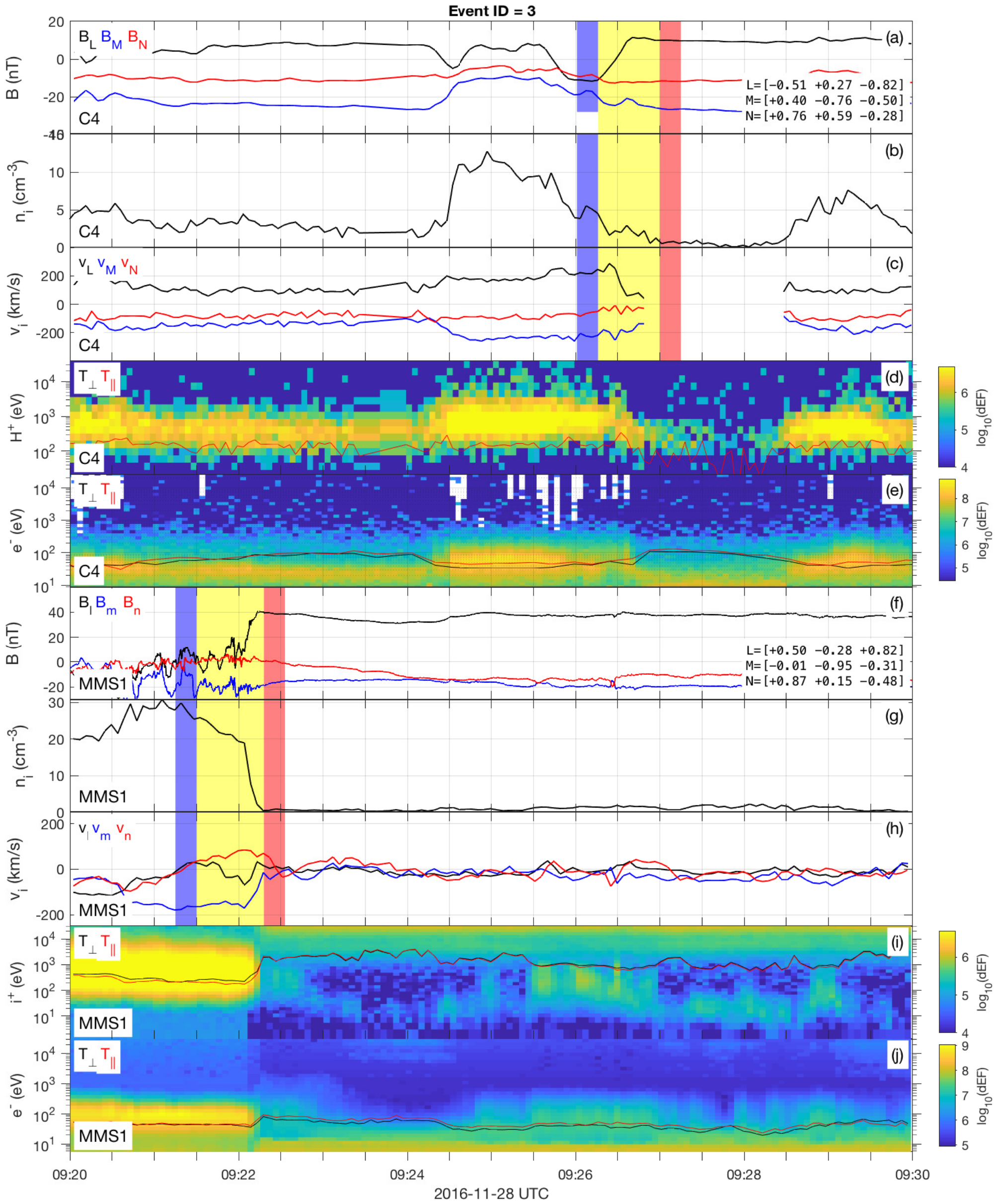

Figure S1. MMS and Cluster simultaneous observations of the magnetopause during event 3 (see Table 1). The yellow-shaded regions mark the time interval used to apply MVA to the current sheet crossing and obtain the LMN coordinate system for each spacecraft. Blue-shaded and red-shaded regions mark the intervals used as reference for the asymptotic conditions of the magnetosheath and the magnetosphere, respectively. (a) C4 magnetic field in LMN coordinates. (b) C4 ion number density. (c) C4 ion velocity in LMN coordinates. (d) (color) C4 CODIF proton spectrogram in differential Energy Flux units (dEF), keV/(cm^2 s sr keV), (black) perpendicular proton temperature, (red) parallel proton temperature. (e) (color) C4 PEACE electron spectrogram in differential Energy Flux units (dEF), keV/(cm^2 s sr keV), (black) perpendicular electron temperature, (red) parallel electron temperature. (f) MMS1 magnetic field in LMN coordinates. (g) MMS1 ion number density. (h) MMS ion velocity in LMN coordinates. (i) (color) MMS1 FPI ion spectrogram in differential Energy Flux units (dEF), keV/(cm^2 s sr keV), (black) perpendicular ion temperature, (red) parallel ion temperature. (j) (color) MMS1 FPI electron spectrogram in differential Energy Flux units (dEF), keV/(cm^2 s sr keV), (black) perpendicular electron temperature, (red) parallel electron temperature.

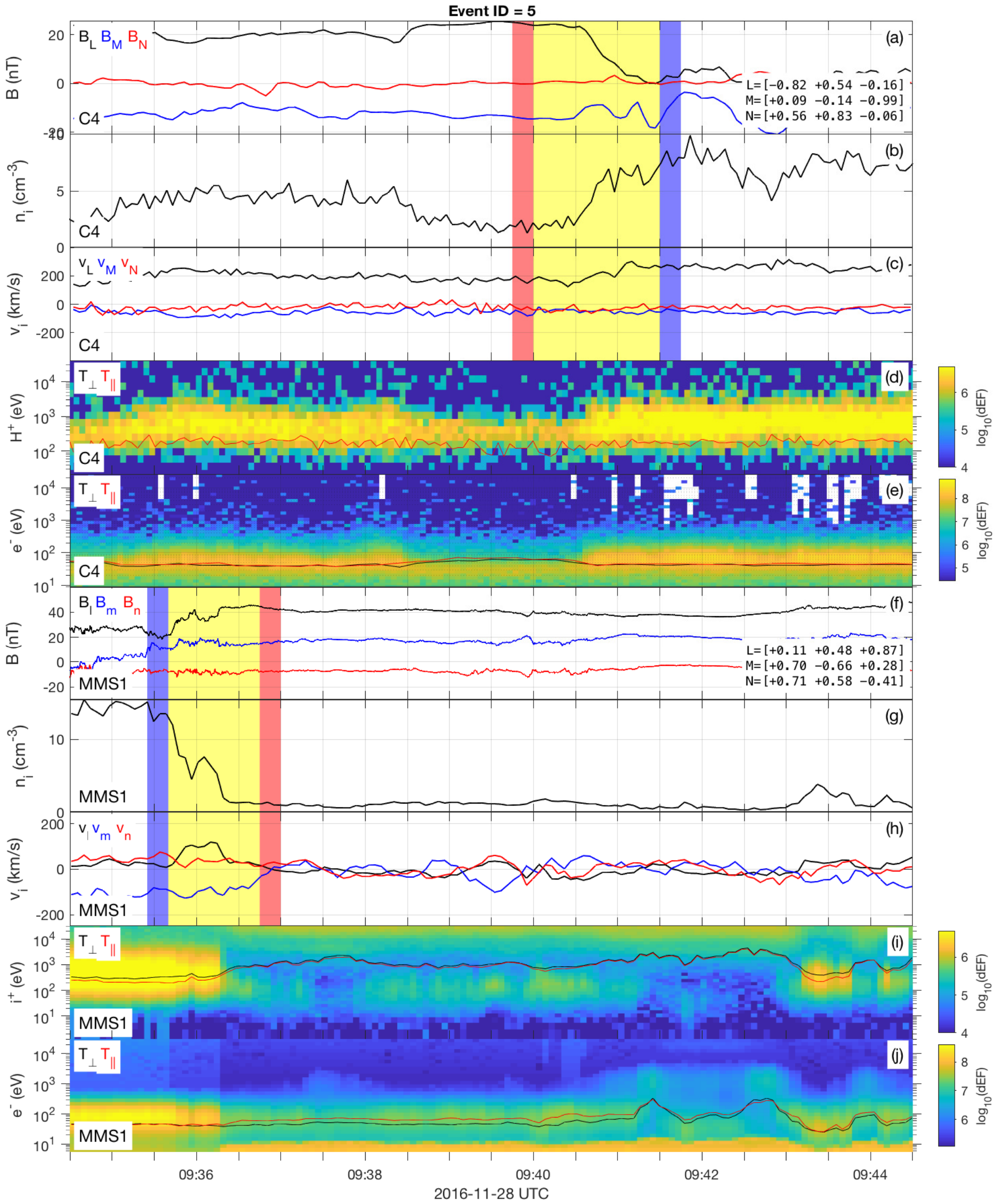

Figure S2. MMS and Cluster simultaneous observations of the magnetopause during event 5 (see Table 1). The yellow-shaded regions mark the time interval used to apply MVA to the current sheet crossing and obtain the LMN coordinate system for each spacecraft. Blue-shaded and red-shaded regions mark the intervals used as reference for the asymptotic conditions of the magnetosheath and the magnetosphere, respectively. (a) C4 magnetic field in LMN coordinates. (b) C4 ion number density. (c) C4 ion velocity in LMN coordinates. (d) (color) C4 CODIF proton spectrogram in differential Energy Flux units (dEF), keV/(cm^2 s sr keV), (black) perpendicular proton temperature, (red) parallel proton temperature. (e) (color) C4 PEACE electron spectrogram in differential Energy Flux units (dEF), keV/(cm^2 s sr keV), (black) perpendicular electron temperature, (red) parallel electron temperature. (f) MMS1 magnetic field in LMN coordinates. (g) MMS1 ion number density. (h) MMS ion velocity in LMN coordinates. (i) (color) MMS1 FPI ion spectrogram in differential Energy Flux units (dEF), keV/(cm^2 s sr keV), (black) perpendicular ion temperature, (red) parallel ion temperature. (j) (color) MMS1 FPI electron spectrogram in differential Energy Flux units (dEF), keV/(cm^2 s sr keV), (black) perpendicular electron temperature, (red) parallel electron temperature.

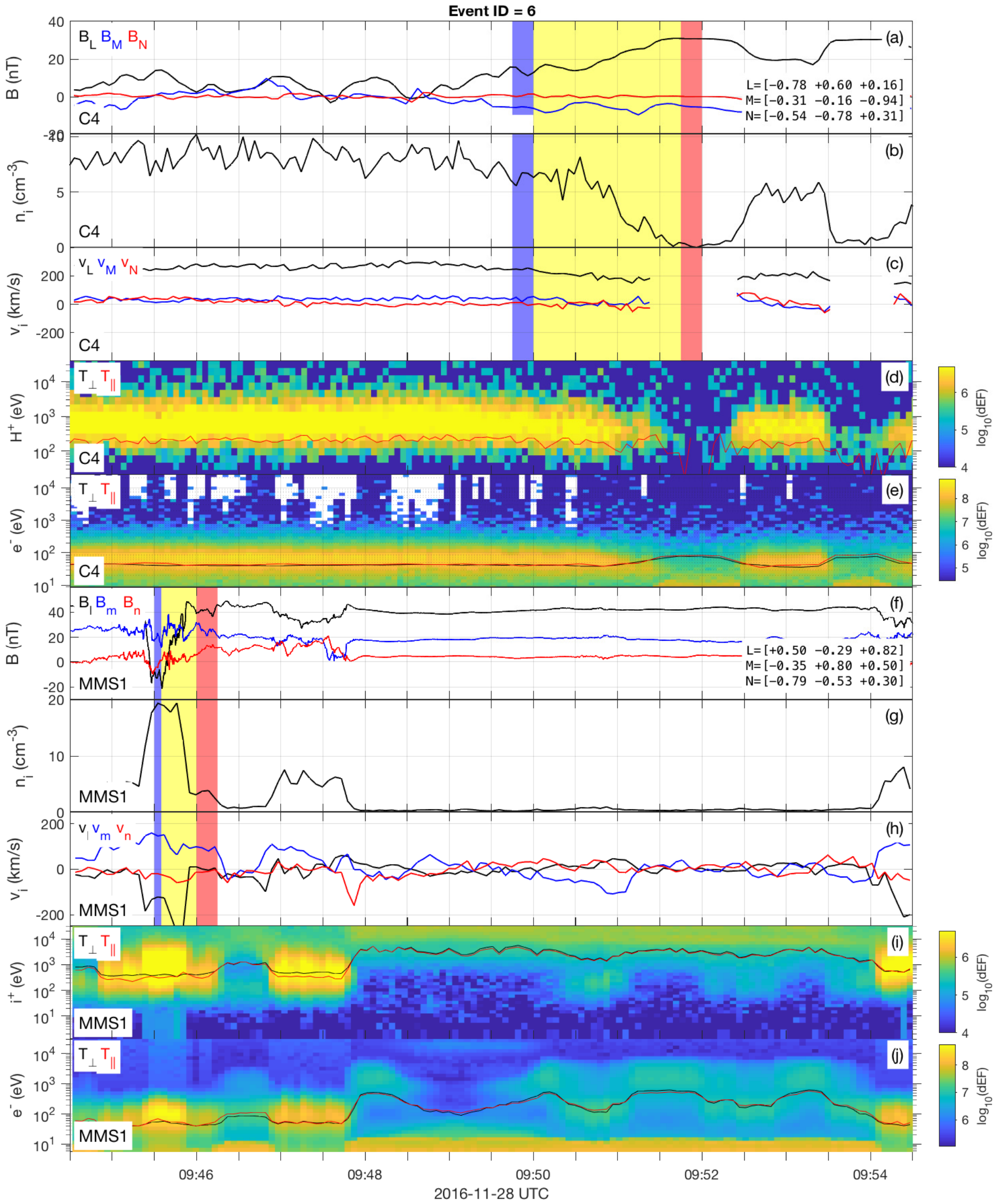

Figure S3. MMS and Cluster simultaneous observations of the magnetopause during event 6 (see Table 1). The yellow-shaded regions mark the time interval used to apply MVA to the current sheet crossing and obtain the LMN coordinate system for each spacecraft. Blue-shaded and red-shaded regions mark the intervals used as reference for the asymptotic conditions of the magnetosheath and the magnetosphere, respectively. (a) C4 magnetic field in LMN coordinates. (b) C4 ion number density. (c) C4 ion velocity in LMN coordinates. (d) (color) C4 CODIF proton spectrogram in differential Energy Flux units (dEF), keV/(cm^2 s sr keV), (black) perpendicular proton temperature, (red) parallel proton temperature. (e) (color) C4 PEACE electron spectrogram in differential Energy Flux units (dEF), keV/(cm^2 s sr keV), (black) perpendicular electron temperature, (red) parallel electron temperature. (f) MMS1 magnetic field in LMN coordinates. (g) MMS1 ion number density. (h) MMS ion velocity in LMN coordinates. (i) (color) MMS1 FPI ion spectrogram in differential Energy Flux units (dEF), keV/(cm^2 s sr keV), (black) perpendicular ion temperature, (red) parallel ion temperature. (j) (color) MMS1 FPI electron spectrogram in differential Energy Flux units (dEF), keV/(cm^2 s sr keV), (black) perpendicular electron temperature, (red) parallel electron temperature.

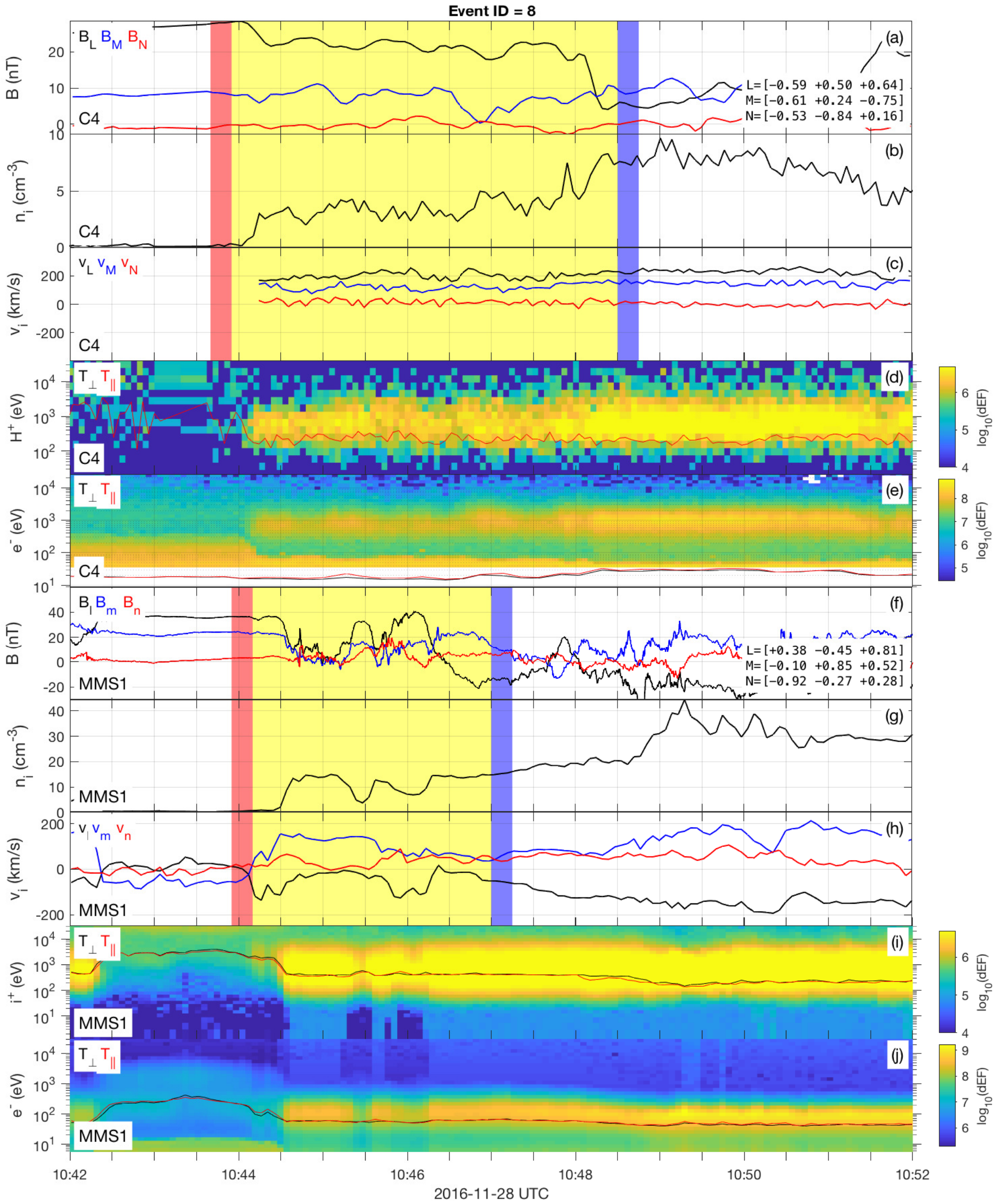

Figure S4. MMS and Cluster simultaneous observations of the magnetopause during event 8 (see Table 1). The yellow-shaded regions mark the time interval used to apply MVA to the current sheet crossing and obtain the LMN coordinate system for each spacecraft. Blue-shaded and red-shaded regions mark the intervals used as reference for the asymptotic conditions of the magnetosheath and the magnetosphere, respectively. (a) C4 magnetic field in LMN coordinates. (b) C4 ion number density. (c) C4 ion velocity in LMN coordinates. (d) (color) C4 CODIF proton spectrogram in differential Energy Flux units (dEF), keV/(cm^2 s sr keV), (black) perpendicular proton temperature, (red) parallel proton temperature. (e) (color) C4 PEACE electron spectrogram in differential Energy Flux units (dEF), keV/(cm^2 s sr keV), (black) perpendicular electron temperature, (red) parallel electron temperature. (f) MMS1 magnetic field in LMN coordinates. (g) MMS1 ion number density. (h) MMS ion velocity in LMN coordinates. (i) (color) MMS1 FPI ion spectrogram in differential Energy Flux units (dEF), keV/(cm^2 s sr keV), (black) perpendicular ion temperature, (red) parallel ion temperature. (j) (color) MMS1 FPI electron spectrogram in differential Energy Flux units (dEF), keV/(cm^2 s sr keV), (black) perpendicular electron temperature, (red) parallel electron temperature.

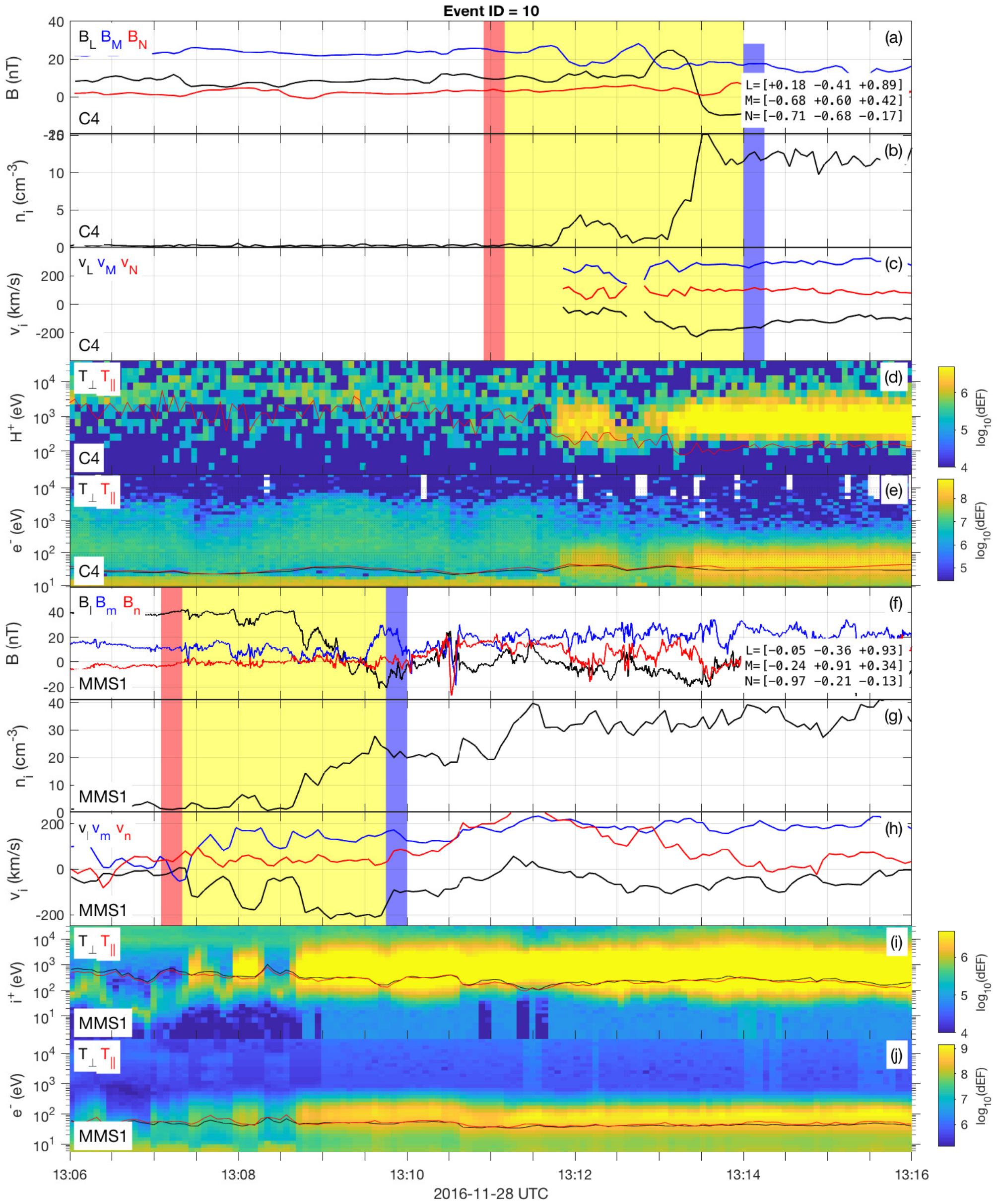

Figure S5. MMS and Cluster simultaneous observations of the magnetopause during event 8 (see Table 1). The yellow-shaded regions mark the time interval used to apply MVA to the current sheet crossing and obtain the LMN coordinate system for each spacecraft. Blue-shaded and red-shaded regions mark the intervals used as reference for the asymptotic conditions of the magnetosheath and the magnetosphere, respectively. (a) C4 magnetic field in LMN coordinates. (b) C4 ion number density. (c) C4 ion velocity in LMN coordinates. (d) (color) C4 CODIF proton spectrogram in differential Energy Flux units (dEF), keV/(cm^2 s sr keV), (black) perpendicular proton temperature, (red) parallel proton temperature. (e) (color) C4 PEACE electron spectrogram in differential Energy Flux units (dEF), keV/(cm^2 s sr keV), (black) perpendicular electron temperature, (red) parallel electron temperature. (f) MMS1 magnetic field in LMN coordinates. (g) MMS1 ion number density. (h) MMS ion velocity in LMN coordinates. (i) (color) MMS1 FPI ion spectrogram in differential Energy Flux units (dEF), keV/(cm^2 s sr keV), (black) perpendicular ion temperature, (red) parallel ion temperature. (j) (color) MMS1 FPI electron spectrogram in differential Energy Flux units (dEF), keV/(cm^2 s sr keV), (black) perpendicular electron temperature, (red) parallel electron temperature.

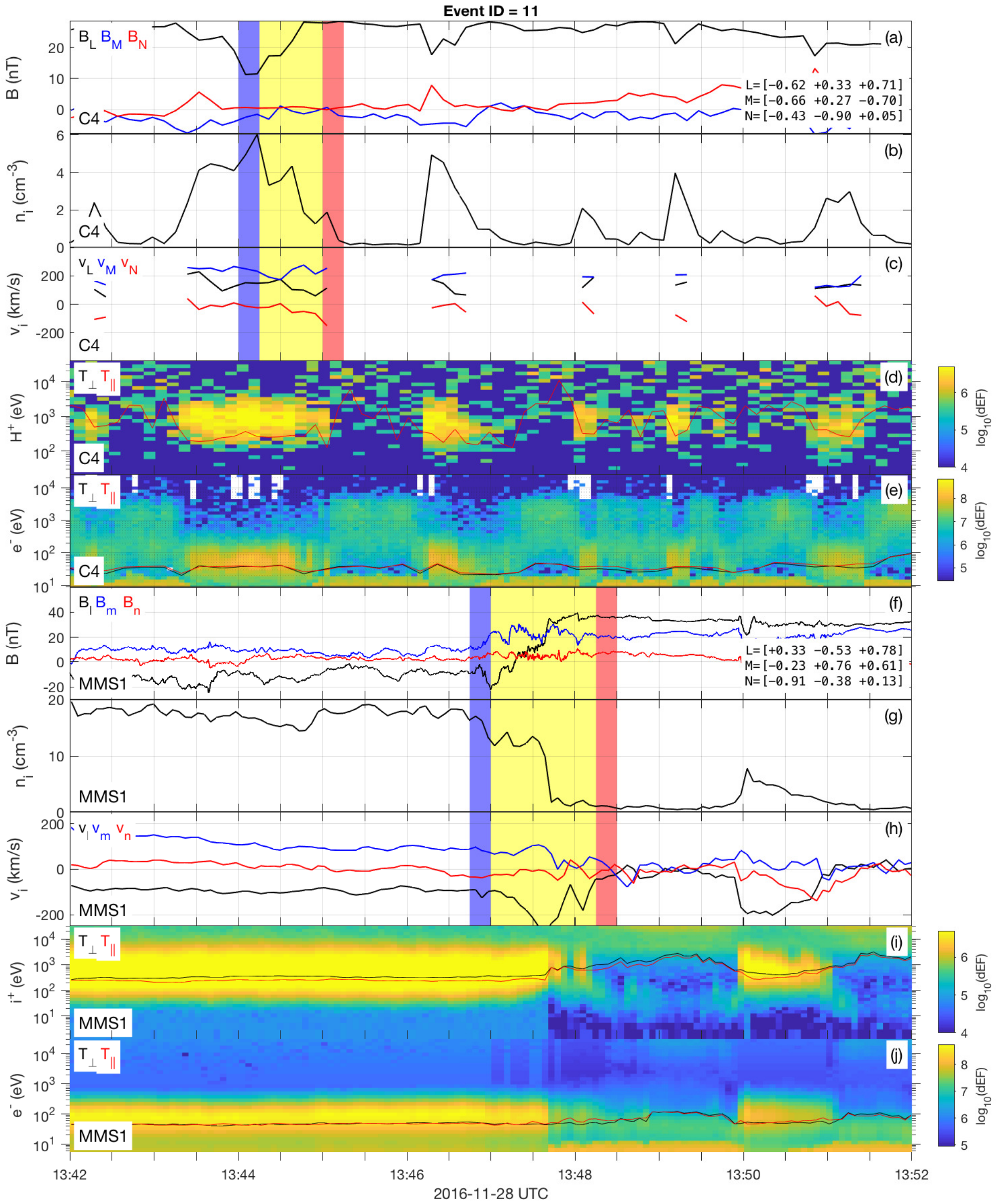

Figure S6. MMS and Cluster simultaneous observations of the magnetopause during event 8 (see Table 1). The yellow-shaded regions mark the time interval used to apply MVA to the current sheet crossing and obtain the LMN coordinate system for each spacecraft. Blue-shaded and red-shaded regions mark the intervals used as reference for the asymptotic conditions of the magnetosheath and the magnetosphere, respectively. (a) C4 magnetic field in LMN coordinates. (b) C4 ion number density. (c) C4 ion velocity in LMN coordinates. (d) (color) C4 CODIF proton spectrogram in differential Energy Flux units (dEF), keV/(cm^2 s sr keV), (black) perpendicular proton temperature, (red) parallel proton temperature. (e) (color) C4 PEACE electron spectrogram in differential Energy Flux units (dEF), keV/(cm^2 s sr keV), (black) perpendicular electron temperature, (red) parallel electron temperature. (f) MMS1 magnetic field in LMN coordinates. (g) MMS1 ion number density. (h) MMS ion velocity in LMN coordinates. (i) (color) MMS1 FPI ion spectrogram in differential Energy Flux units (dEF), keV/(cm^2 s sr keV), (black) perpendicular ion temperature, (red) parallel ion temperature. (j) (color) MMS1 FPI electron spectrogram in differential Energy Flux units (dEF), keV/(cm^2 s sr keV), (black) perpendicular electron temperature, (red) parallel electron temperature.

Table S1. Asymptotic conditions at dusk flank (C4) and subsolar region (MMS1)

ID	SC	L	N	Magnetosphere[a]		Magnetosheath[a]		v_A^b	$v_{s,L}^c$	$\Delta\beta$	B clock angle[d]
		(GSE)	(GSE)	B_L (nT)	n (cm^{-3})	B_L (nT)	n (cm^{-3})	(km/s)	(km/s)		(deg)
3	C4	-0.51 +0.27 -0.82	+0.76 +0.59 -0.28	10	0.6	-11	4.7	338	225	0.6	52
	MMS	+0.50 -0.28 +0.82	+0.87 +0.15 -0.48	39	0.8	6	27.6	124	16	9.8	45
5	C4	-0.82 +0.54 -0.16	+0.56 +0.83 -0.06	24	1.9	2	7.8	146	262	5.8	46
	MMS	+0.11 +0.48 +0.87	+0.71 +0.58 -0.41	43	1.2	21	13.6	249	15	2.1	9
6	C4	-0.78 +0.60 +0.16	-0.54 -0.78 +0.31	31	0.1	13	6.3	221	248	2.5	13
	MMS	+0.50 -0.29 +0.82	-0.79 -0.53 +0.30	41	3.4	-11[e]	19.3[e]	188	1	5.7	88
8	C4	-0.59 +0.50 +0.64	-0.53 -0.84 +0.16	28	0.2	5	7.6	159	223	7.2	41
	MMS	+0.38 -0.45 +0.81	-0.92 -0.27 +0.28	36	0.6	-14	15.3	187	51	7.3	112
10	C4	+0.18 -0.41 +0.89	-0.71 -0.68 -0.17	9	0.2	-8	12.3	187	163	1.4	44
	MMS	-0.05 -0.36 +0.93	-0.97 -0.21 -0.13	40	1.2	-10	21.3	169	100	4.4	102
11	C4	-0.62 +0.33 +0.71	-0.43 -0.90 +0.05	28	1.1	11	5.5	192	150	4.5	9
	MMS	+0.33 -0.53 +0.78	-0.91 -0.38 +0.13	36	1.1	-10	15.5	177	71	6.1	95
15	C4	+0.36 -0.55 +0.76	-0.48 -0.80 -0.35	15	0.2	-11	7.1	228	116	0.2	82
	MMS	+0.24 -0.34 +0.91	-0.64 -0.76 -0.12	43	0.6	-12	26.4	223	86	2.5	82

[a] Averaged values over 15 s adjacent to the magnetopause current sheet.
[b] Hybrid Alfvén velocity (Cassak & Shay, 2007).
[c] Shear flow speed parallel to the outflow (L) direction.
[d] Rotation angle in the LM plane.
[e] Averaged values over 5 s, see Figure S3.